



## Supplementary Materials for

### **Anthropogenic climate change has influenced global river flow seasonality**

Hong Wang *et al.*

Corresponding author: Junguo Liu, liujg@sustech.edu.cn

*Science* **383**, 1009 (2024)  
DOI: 10.1126/science.adl9501

#### **The PDF file includes:**

Materials and Methods  
Figs. S1 to S18  
Tables S1 to S3  
References

## Materials and Method

### Observation-based datasets

Monthly river flow time series (calculated from daily records) were obtained from the Global Streamflow Indices and Meta data archive (GSIM) (18, 46, 51). The Global Runoff Data Centre (52) (GRDC) database, offering river flow at monthly scale that are excluded by GSIM, are used as a complementary dataset. To compute RFS with minimal bias, two selection standards were formulated: i) the study period ranges from 1965 to 2014 to ensure sufficient stations for analysis with wide spatial coverage; ii) monthly discharge is used to calculate annual seasonality index only when there are 10 or more months of data available in a year. Given rapidly changing climate, we extended our analysis to include more recent years by combining five regularly updated river flow datasets (Table S3) from national to global level for 2017-2019. All GRDC stations in countries that have a national or a continental database (e.g. USGS data within the US) were replaced to avoid duplicated time series of river flow when combining datasets.

To achieve a global scale coverage, a recently published global gridded monthly reconstruction of runoff (GRUN) data set was used (19, 47). GRUN is developed from *in-situ* monthly river flow observations from the GSIM with a  $0.5^{\circ}$  spatial resolution covering the period from 1902 to 2014 (19). It is derived by training a machine learning algorithm based on the gridded observations of precipitation and temperature from the Global Soil Wetness Project Phase 3 (GSPWP3) dataset (19), therefore, GRUN is not able to explicitly account for the effects of HWLU. Observed monthly river discharge from the GRDC dataset and multimodel simulations from phase 2a of the Inter-Sectoral Impact Model Intercomparison Project (ISIMIP2a) reconstructions are used for its validation (19). Four additional members in the newly published G-RUN ENSEMBLE which overlap in 1965-2014 were used to account for the uncertainty of atmospheric forcing datasets on runoff, including runoff reconstructions forced with CRUTSv4.04, GSPWP3-W5E5, GSPWP3-EWEMBI and PGFv3 (53). The spatial pattern of AE trends from G-RUN ENSEMBLE coinciding with GRUN supports use of GRUN to conduct climate change detection and attribution analysis and further confirms the robustness of our results (Fig. S17). In summary, *in-situ* observations incorporate the impacts from climate change (including ACC, natural forcing, and natural climate variability) and human activities (such as reservoirs, human water management, and land-use change, abbreviated as HWLU). Instead, GRUN and G-RUN ENSEMBLE only account for the impacts from climate change. To exclude impacts of reservoirs on the spatial pattern of RFS trends from *in-situ* observations, HydroBASIN subbasin units (Pfafstetter level 12) (54) are integrated with degree of regulation (DOR) provided by Grill et al. (55) to distinguish gauge stations into those influenced by reservoirs ( $DOR > 0$ ) and those unaffected by reservoirs ( $DOR = 0$ ). The DOR at the subbasin unit level is represented by selecting the maximum value of DOR at the river reach scale. There are 6,150 stations identified as free from reservoir influence, while 3,914 stations are situated in subbasins or downstream of reservoirs (with 49 stations located outside the HydroBASINS range due to their presence on islands, and another 7 stations lacking DOR information).

Snow-dominated regions were identified worldwide by the average snow to precipitation ratio in the period 1979-2000 from the WFDE5 dataset (56), which contains global precipitation and snow flux at a resolution of  $0.5^{\circ}$ . Time series of snow fraction during 1965-2014 is calculated from the fifth-generation atmospheric reanalysis (ERA5) for full time coverage (57). To rule out precipitation seasonality, observed monthly gridded precipitation data from the Global Precipitation Climatology Centre (GPCC) (58) at a resolution of  $2.5 \times 2.5^{\circ}$  for the period of 1965-2014 at monthly scale was used. Mean air temperature data from the CRUTEM5 dataset at a resolution of  $5 \times 5^{\circ}$  for the period 1965–2014 were used (59). The

permafrost and glacier maps are from the International Permafrost Association (IPA) and Randolph Glacier Inventory (RGI) (60, 61).

### Model simulations

We used the ISIMIP simulation round 2b (ISIMIP2b) outputs of global daily discharge to investigate whether ACC impacts on RFS can be detected. Seven global hydrological models (GHMs) (CLM4.5, H08, MATSIRO, MPI-HM, LPJmL, PCR-GLOBWB and WaterGAP2) under the framework of ISIMIP2b were obtained (62). Each GHMs is run under different climate scenarios with different social and economic scenarios in four bias-corrected global climate models (GCMs) contributing to the Coupled Model Intercomparison Project 5 (CMIP5) archive, except for MPI-HM (only three GCMs, Table S2), thereby providing us with 27 GCM-GHM combination datasets of gridded daily discharge. All models considered water consumption sectors (for irrigation / domestic / industrial purposes), reservoir management, and land-use change, apart from CLM45 and MPI-HM, which only considered irrigation water use without reservoir operation. The scenarios of GCM-GHM combinations considered are listed below (Table S2):

1. Picontrol&1860soc: pre-industrial control (Picontrol, including natural climatic variability) simulations under 1860 social and economic scenarios (1860soc) run from 1661-1860. All available Picontrol&1860soc simulations were split into non-overlapping 50-year segments, resulting in a total of 108 segments, to account for natural climate variability. This simulation is used in the subsequent climate change detection and attribution method.

2. Picontrol&HWLU: the Picontrol simulations run from 1861-2005 are used to drive GHMs that account for HWLU, which do not account for ACC. For 1965-2005, the simulations are forced with histsoc (except for CLM45 with 2005soc). For 2006-2014, HWLU is kept at the constant level of 2005soc.

3. HIST&HWLU: simulations under historical climate forcing (HIST, including anthropogenic climate forcing, natural forcing, and natural climatic variability) are used to drive GHMs that account for HWLU. For 2006-2014/2006-2019, the medium-high emission scenarios (Representative Concentration Pathway (RCP) 6.0) is used to extend the study period (36).

To understand the effect of soil moisture on RFS, monthly gridded soil moisture modeled data from the Climate Prediction Center (CPC) soil moisture dataset for the period 1965–2014 were analyzed. These data are monthly averaged soil moisture water height equivalents with a spatial resolution of 0.5°.

### Seasonality index

After acquisition of data, both the reconstructed and modelled data were interpolated to a  $2.5 \times 2.5^\circ$  grid using the second-conservative regridding method from their respective original grids. We assessed the seasonal variation of monthly river flow using an information theory metric known as Apportionment Entropy (AE). This metric is non-parametric and may even encompass high-order moments, in contrast to other seasonality indices based on standard deviation, Fourier decomposition, and circular statistics (13–15, 22). AE is therefore very well suited to analyzing river discharge distributions globally. Moreover, information theory metrics have been widely used as a measure of rainfall seasonality in both hydrologic and climatological contexts (21, 22). In our case, higher AE values imply lower seasonal variation, and lower AE imply higher seasonal variation.

To estimate AE of river flow over the year k, we firstly calculated the sum of monthly values  $x_m$  ( $m=1,2,\dots,12$ ) in year k, denoted as  $X_k$ .

$$X_k = \sum_{m=1}^{12} x_{m,k} \quad (1)$$

The AE at year k can be calculated as (20):

$$AE_k = - \sum_{m=1}^{12} \frac{x_{m,k}}{X_k} \log_2 \left( \frac{x_{m,k}}{X_k} \right) \quad (2)$$

which by definition, when monthly river flow is uniformly distributed, river flow is equal in each month, and AE reaches its maximum,  $\log_2 12$ . In contrast, if the annual river flow is concentrated in one month and there is no discharge for the rest of the months,  $AE = 0$ .

Anomalies of annual AE were computed by subtracting the long-term mean over the full 1965–2014/1970–2019 period for each station or grid cell. All datasets were masked for overlapping pixels between observational reconstructions and model simulations to achieve the same spatial coverage. We directly use GRUN runoff to calculate RFS, since river flow can be assumed to equal the runoff multiplied by the drainage area (area weighted discharge) at a monthly timescale, where water losses through e.g. channel evaporation are negligible except for in few very large basins (19).

AE characterized the magnitude change of the RFS. Our findings suggest that the trends in river flow timing may not be significant at the stations with significant AE trends included in our analysis, particularly at a monthly scale. This is because flow changes in no high-flow months offset the shift in the centroid timing of river flow (Fig. S5).

### Trend and reliability analysis

Sen's slope is a robust and nonparametric method to reflect time series trends, commonly used in hydro-meteorological analysis to estimate linear trends (63). Stahl et al. developed a method using the Sen's slope  $k$  to calculate change ratio expressed in units of percent change per decade to represent trend magnitudes (64):

$$\text{change ratio} = \frac{k \cdot 10}{\bar{x}} * 100 \quad (3)$$

where  $\bar{x}$  is the mean discharge in the study period. This method is robust to outliers (64). In addition, trend estimates from catchments with different sizes and climate are comparable with this method (51). Significance of trends is estimated by the Mann-Kendall statistical test (65).

Previous literature suggested that trend analysis can be considered when at least 70% of the data-years for stations are available (51). However, long-term hydrological data are deficient in high latitudes, where RFS is stronger. To overcome this lack of long-term station-based river flow observations, the length of record (LOR) method is adopted to characterize the uncertainty associated with the application of shorter record lengths when data are limited (65, 66). This LOR analysis was used to determine how many years of data were required to achieve a specified level of statistical certainty for any flow gauging station (66). Here, a 90% confidence interval for data to be within 5% of the long-term mean was selected to define AE uncertainty. To do this, the whole available period for each station was used to assess the variability of river flow AE and determine the length of record required in calculations when there are at least 35 years record with at least 20 years in the period being studied. Finally, the AE trend was calculated only when there are i)  $\geq 35$  years (70% of the 1965–2014/1970–2019 time period) available or ii)  $\geq 20$  years but no more than 20 years record length was required to constrain AE to be within 5% of the long-term mean with 90%

confidence interval. Typically, large rivers flowing through flat lowlands required shorter record lengths to represent the flow regime because their discharge is characterized with relatively lower intra-and interannual variability than highland streams (66).

### Interpreting AE from high and low flows

To understand the trends of seasonal variability of river flow qualitatively, the annual mean trends of river flow were also included to help identify potential reasons for seasonal variations of river flow for global regions. To interpret the results, low- (high-) flow months were defined as three calendar months when the long-term monthly means of river flow is lowest (highest). Here, we developed a suite of six alteration metrics ascribed as  $T_{LH}$  (trends of low flows and high flows) ( $L-H^*$ ,  $L-H^+$ ,  $L^*H^+$ ,  $L^*H^-$ ,  $L+H^-$ ,  $L+H^*$ ) based on the change directions of AE and the signs and significance of annual mean river flow changes, dividing gauges into six distinct categories. Notation – and + represent the change direction of river flow in low- and high- flow month, \* indicates that the change is not predominant. Only stations with significant AE trends were considered. Therefore, we excluded  $L+H^+$ ,  $L-H^-$ , and  $L^*H^*$  as we assumed stations with significant AE trends would not exhibit the same predominant changes in both low- and high- flow months.

The significant seasonal variations ( $p < 0.05$ ) of river flow at each gauge can be attributed to the variations of high flows and low flows. For example, a station with a significant ( $p < 0.05$ ) increasing AE trend and insignificant ( $p > 0.05$ ) annual mean river flow trend can be assigned to  $L+H^-$  (increasing low flows and decreasing high flows).

Specifically,  $L-H^*$  indicates that decreasing low flows is dominant assuming that both annual mean river flow and AE are experiencing significantly decreasing trends,  $L-H^+$  indicates decreasing low flows and increasing high flows contribute to the significant decreasing trends of AE with insignificant annual mean trends,  $L^*H^+$  indicates that increasing high flows is prominent in the situation of decreasing AE and increasing annual mean trends,  $L^*H^-$  indicates that decreasing high flows is prominent under the condition of significantly increasing AE and decreasing annual mean trends, and  $L+H^*$  indicates low flows are significantly increasing in the case of significantly increasing AE and annual mean trends. A few stations with significant AE trends, such as  $L+H^+$  in the upper Midwest of CONUS and  $L-H^-$  in southeast Brazil, are outside our classification framework. Nevertheless, there is still a predominant change in low- or high-flow months overall, which would result in a significant RFS trend (Fig. S5).

### Climate change detection and attribution

To quantify possible influences of external forcings in the observed/reconstructed RFS, we conducted climate change detection and attribution analyses on AE over the NHL (above 50°N) over the 1965-2014/1970-2019 period. We used two methods to test robustness of the results: one is a correlation-based method (17, 32, 33) and the other is the optimal fingerprinting approach (67) with a regularized covariance estimate (34).

The correlations between the multimodel mean and the observations / pre-industrial control, that is  $\text{corr}(\text{HIST}, \text{obs})$  and  $\text{corr}(\text{Picontrol}, \text{HIST})$ , respectively, quantifies the similarity between the estimated response to human-induced climate change and the observed response or a consequence of natural climate variability (17, 32, 33). The null hypothesis is that there is no signal in the observations resulting from human-induced climate change, that is, the  $\text{corr}(\text{HIST}, \text{obs})$  will be approximately zero and not distinguishable from  $\text{corr}(\text{Picontrol}, \text{HIST})$ . On the contrary, if  $\text{corr}(\text{HIST}, \text{obs})$  is significantly larger than zero, e.g. greater than almost all the estimates of  $\text{corr}(\text{Picontrol}, \text{HIST})$ , then the null hypothesis is rejected with high confidence. This indicates that the observed response includes a signal stemming from the external forcing given by human-induced climate change. A normal

distribution using the mean and standard deviation of  $\text{corr}(\text{Picontrol}, \text{HIST})$  was assumed for providing the 95% and 99% confidence levels in comparison with  $\text{corr}(\text{HIST}, \text{obs})$  (32, 33).

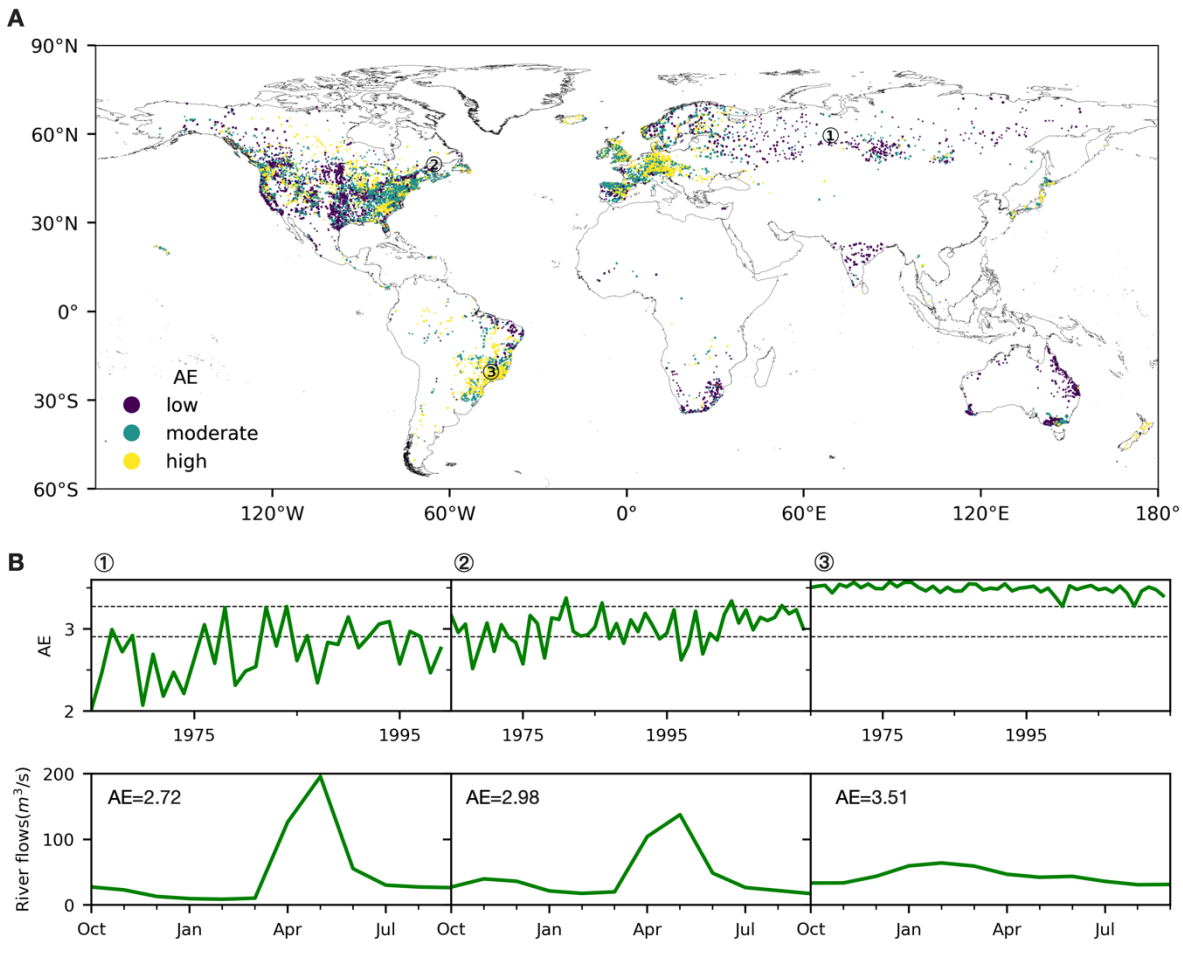
For the correlation approach, all available Picontrol simulations were used and divided into multiple nonoverlapping 50-year segments with the last segment discarded if shorter than 50 years to match the time span of our study period, providing 216 ( $8 \times 27$ ) chunks of Picontrol simulations span 1661–2099 in total. It is noted that there is no difference if we exclude Picontrol&1860soc simulations in the correlation method (Fig. S18), since the impacts of HWLU on RFS are underrepresented in simulations (Fig. 3C). The Spearman correlation coefficient was used because of its resistance to outliers.

We used the correlation method to examine the spatial and temporal consistency of AE changes between the multimodel mean of historical simulations and the observation, as opposed to estimates from Picontrol. We did this by comparing spatial  $\text{corr}(\text{HIST}, \text{obs})$  with spatial  $\text{corr}(\text{Picontrol}, \text{HIST})$  of AE trends (%/decade), denoted as  $\text{corr}_{\text{spatial}}(\text{HIST}, \text{obs})$  and  $\text{corr}_{\text{spatial}}(\text{Picontrol}, \text{HIST})$ , distinguished from the temporal correlation coefficient of AE anomalies, denoted as  $\text{corr}_{\text{temporary}}(\text{HIST}, \text{obs})$  and  $\text{corr}_{\text{temporary}}(\text{Picontrol}, \text{HIST})$ .

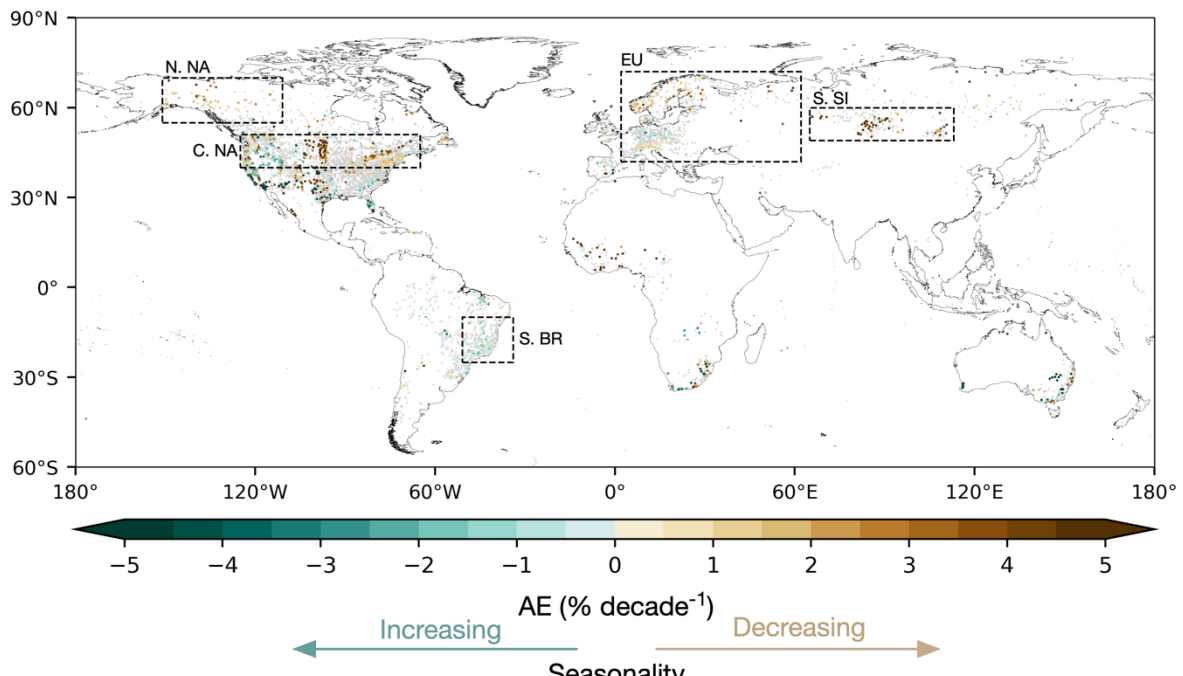
Optimal fingerprinting was applied to detect and attribute changes in the observational reconstructed magnitude of the AE in the NHL (above 50°N) from 1965-2014/1970-2019. The optimal fingerprint method is based on the generalized linear regression of the observed or reconstructed AE as a combination of climate responses to external forcing plus internal variability (34). The regression model for the one-signal climate change detection and attribution analysis is:

$$\begin{cases} y = x^* \beta + \varepsilon \\ x = x^* + v \end{cases} \quad (4)$$

where observation vector  $y$  and the simulation ensemble average response matrix  $x$  are known, the actual regressor of  $x^*$  in response to external climate forcing can be obtained with the noise term  $v$ .  $v$  represents the effect of internal variability that remains in  $x$  resulting from sampling since multimodel averaging of forced runs cannot remove all internal variability because the size of the latter is usually small. The observations are acquired from the actual regressor  $x^*$  by multiplying the scaling factor  $\beta$  plus the noise term  $\varepsilon \sim N(0, \Sigma)$ , with  $\Sigma$  being a covariance matrix derived from 108 ( $27 \times 4$ ) groups of unforced Picontrol simulations under 1860soc accounting for natural variability and uncertainty of multimodel means. To derive the best estimate of  $\beta$  and the associated confidence intervals,  $\Sigma$  is divided into two equally independent groups  $\Sigma_1$  and  $\Sigma_2$  following previous research (17, 33). To account for uncertainty of randomly splitting Picontrol&1860soc simulations into two halves, we replicate the procedure 2,000 times, resulting in 2,000  $\beta$  and corresponding 99% confidence intervals. Median of the resamples was considered as best estimate of 0.5-99.5% uncertainty ranges of  $\beta$ . A signal is detected if the lower confidence bound of  $\beta$  is above zero. Furthermore, if the confidence interval of  $\beta$  includes one, the magnitude of the mean response of AE is consistent with the observations. In this study,  $x^*$  is estimated using the ensemble mean of the HIST&HWLU simulations (34). If simulations include the drivers of anthropogenic climate forcing, that is HIST&HWLU, are consistent with the observation, then it is possible to claim attribution. The consistency of the unexplained signal  $\varepsilon$  with internal variability was also assessed using a residual consistency test (RCT) (34). The RCT uses a non-parametric estimation of the null distribution through Monte Carlo simulations, and its  $p$  value is estimated. If  $p > 0.1$ , the RCT passed, which indicates the consistency between the regression residuals and the model-simulated variability (34). The optimal fingerprinting detection and attribution analyses were performed using code provided in ref. (34).



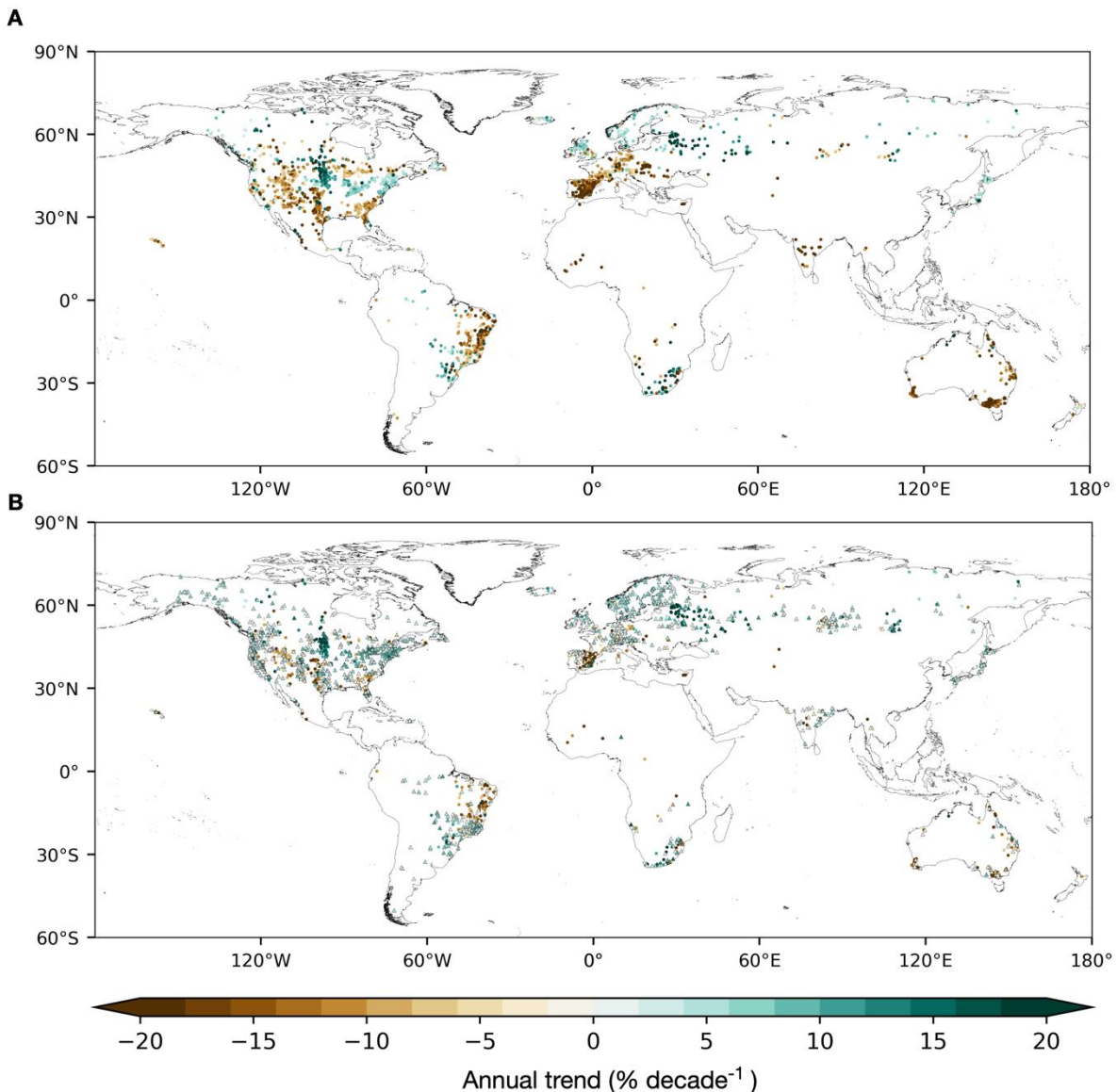
3 Classification of river flow seasonality. (A) Distribution of low, moderate, and high  
4 apportionment entropy (AE), corresponding to high, moderate, and low river flow  
5 seasonality, respectively, based on 30th and 70th percentile of mean AE (2.91 and 3.28, two  
6 dashed lines in (B)) in the 1965-1994 baseline period. (B) Time series of low, moderate, and  
7 high AE corresponding to three types of flow regimes with similar annual mean river flow  
8 ( $40\sim45\text{m}^3/\text{s}$ ) in the stations of ① Bogadinskoje, south Serbia; ② near Fort Kent Maine,  
9 northeast CONUS; and ③ Rio Pardo, southeast Brazil, respectively. 30 years referenced  
10 mean AE are noted in the left corner. River flow observations are not available after 2000 in  
11 Bogadinskoje.



12

13 **Fig. S2.**

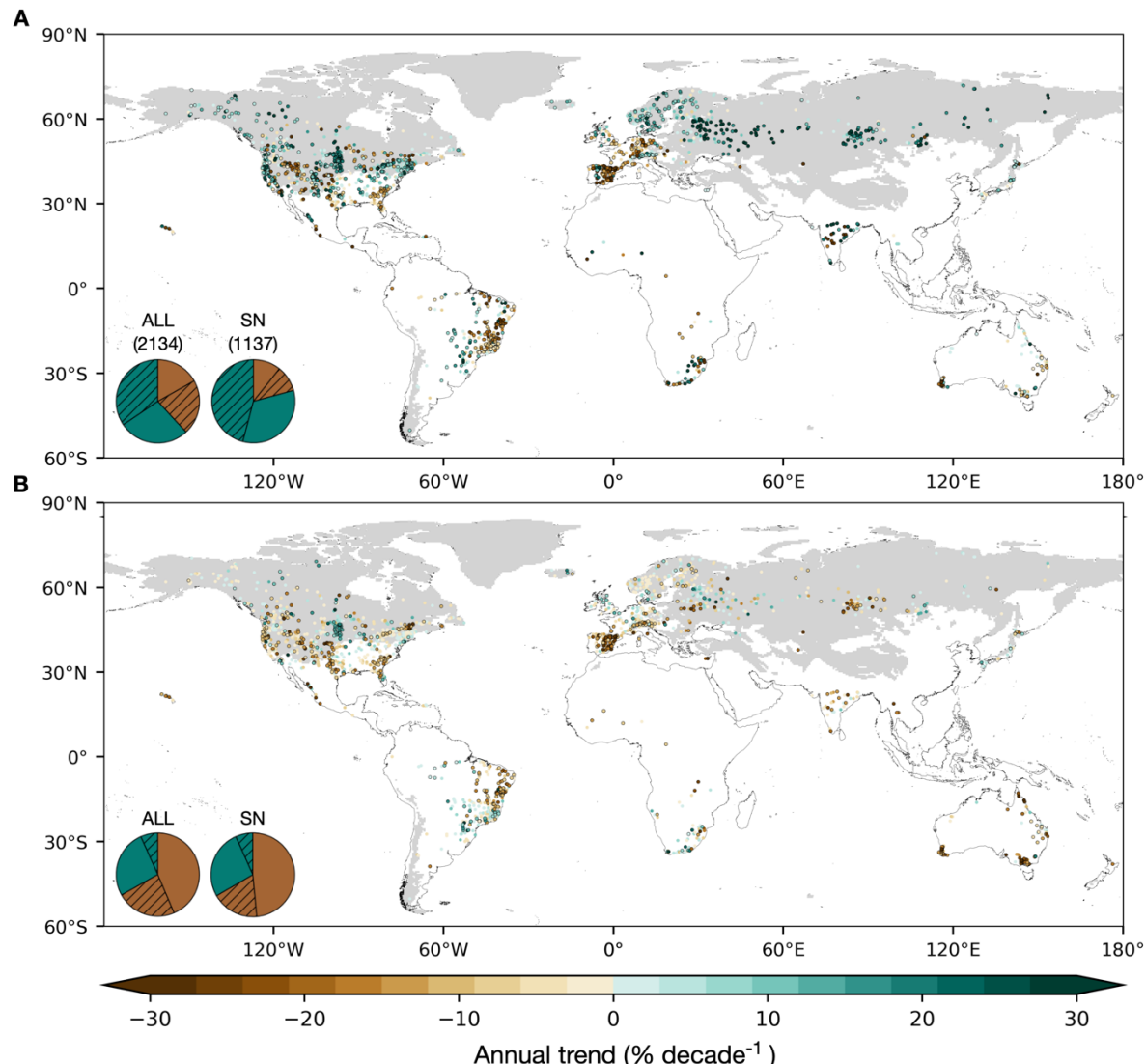
14 River flow seasonality trends represented by apportionment entropy (AE) (% decade<sup>-1</sup>) over  
 15 50 years (1970–2019). Similar to Fig. 1A in the main text, but with study period replaced  
 16 with 1970–2019.



17

18 **Fig. S3.**

19 Trends of annual mean river flow ( $\% \text{ decade}^{-1}$ ) over 50 years (1965-2014) in the stations with  
 20 (A) significant ( $p < 0.05$ ) annual mean trends (2301 stations) or (B) significant ( $p < 0.05$ )  
 21 seasonal trends (2134 stations). In (B), stations without significant annual mean trends  
 22 are represented as black edged triangles, which account for 65% (1380 stations) of the stations  
 23 with significant seasonal trends.



24

25 **Fig. S4.**

26 Trends of river flow in (A) low- and (B) high-flow months (%decade<sup>-1</sup>) over 50 years (1965–  
 27 2014). Stations with significant trends ( $p < 0.05$ ) are circled with black. The number of  
 28 stations included is indicated in parentheses. Regions where snow fraction in precipitation is  
 29 larger than 0.2 are showed in grey as snowmelt-dominated areas. The pie charts depict the  
 30 proportions of stations with significant trends (hatched,  $p < 0.05$ ) and insignificant trends  
 31 (solid) worldwide (ALL) and in the snowmelt-dominated areas (SN).

32  
33  
34  
35  
36  
37  
38  
39  
40  
41  
42  
43

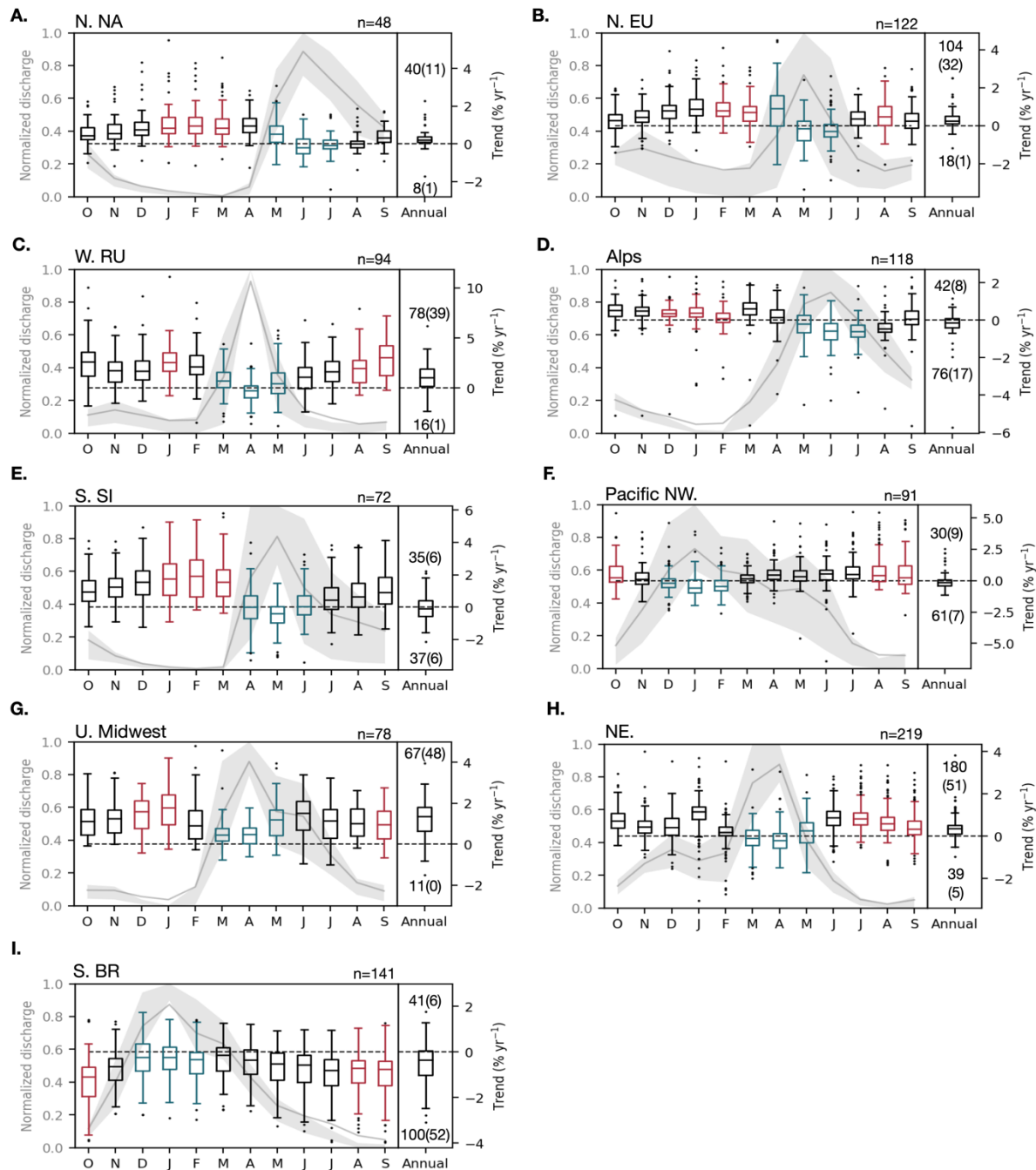
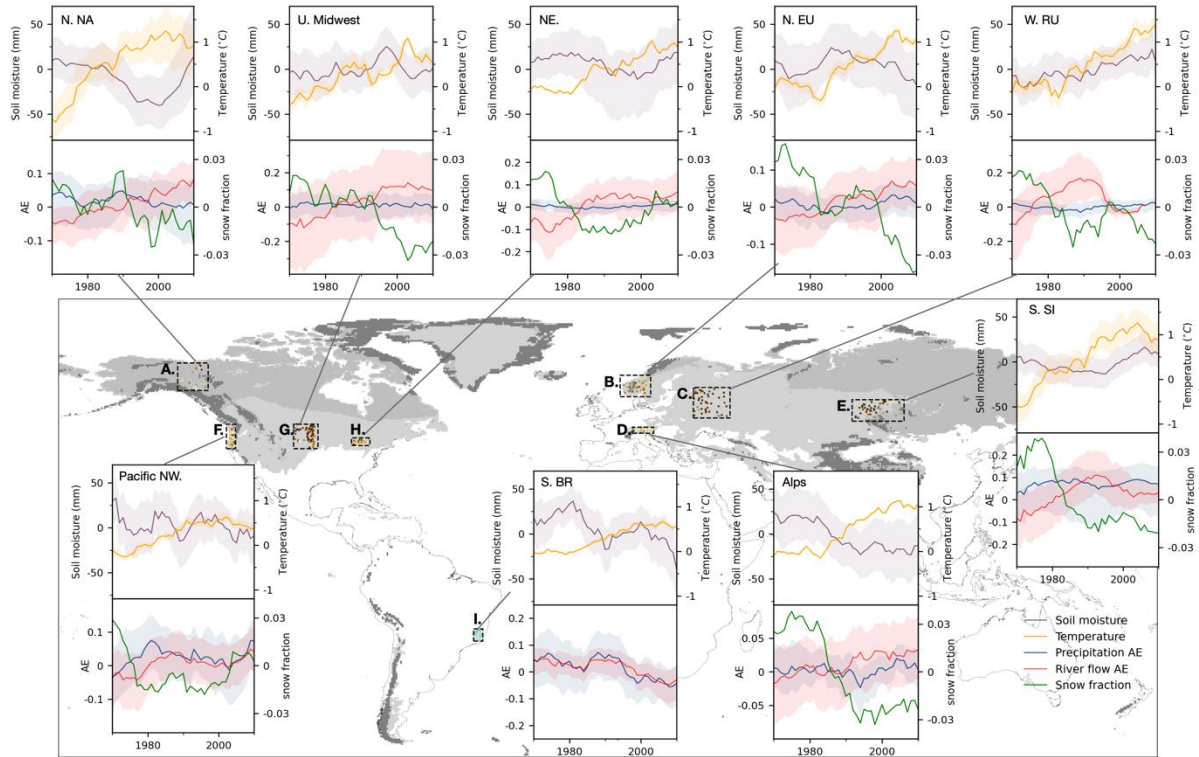


**Fig. S5.**

Normalized monthly mean flow regime (grey line) within the 25th and 75th percentile range (grey shading) and boxplot of monthly and annual mean river flow trends ( $\% \text{ yr}^{-1}$ ) in (A) northern North America, (B) northern Europe, (C) western Russia, (D) higher elevation European Alps, (E) south Siberia, (F) Pacific Northwest, (G) upper Midwest, (H) northeast CONUS, (I) southeast Brazil. Low (high) flow months are defined as three calendar months with lowest long-term monthly means of river flow noted in red (blue). Only stations whose seasonal trends are significant ( $p < 0.05$ ) and the same as the dominant change direction in each region are included in statistics. Numbers within annual boxplots indicate the number of positive and negative trends, excluding trends equal to zero. Numbers in parentheses indicate the count of trends that were significant ( $p < 0.05$ ).

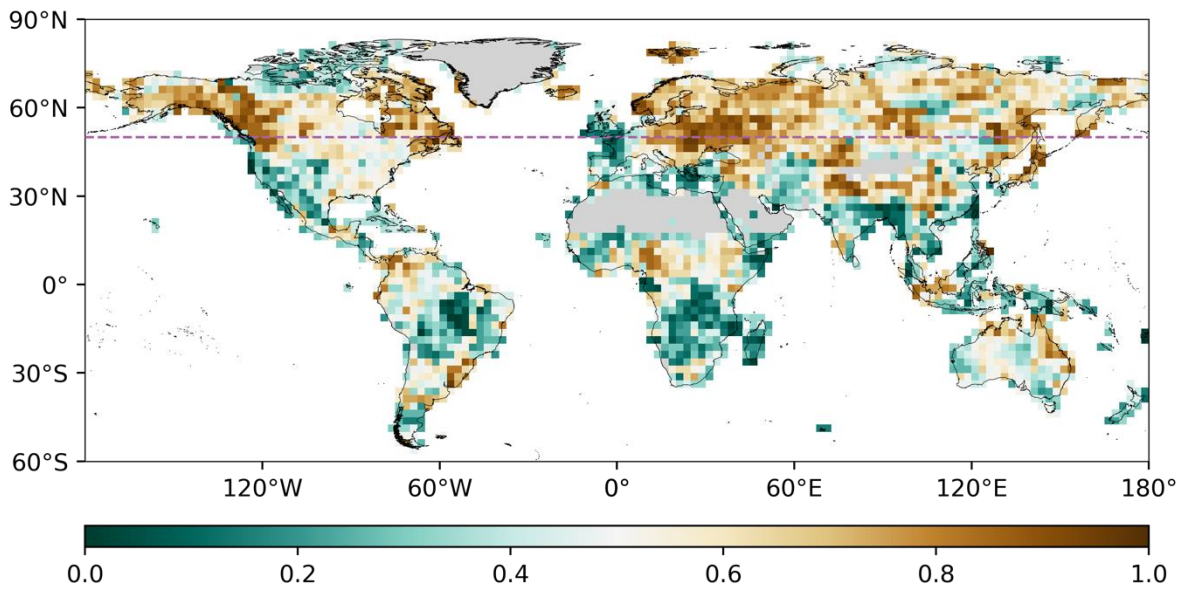
44



45

#### 46 Fig. S6.

47 Temporal evolution of river flow seasonality with their potential climatic drivers for  
 48 subspaces in the nine hotspots in (A) northern North America, (B) northern Europe, (C)  
 49 western Russia, (D) higher elevation European Alps, (E) south Siberia, (F) Pacific Northwest,  
 50 (G) upper Midwest, (H) northeast CONUS, (I) southeast Brazil. Data show anomalies of soil  
 51 moisture in high-flow months (purple), temperature (yellow), precipitation (blue), river flow  
 52 (red) seasonality, and snow fraction (green) changes. Solid lines show the median and shaded  
 53 bands indicate the spatial variability within the subspaces (25th and 75th percentiles). Bands  
 54 are not shown for snow fraction to enhance readability of the plot. Regions where snow  
 55 fraction in precipitation is larger than 0.2 are shown in light grey as snowmelt-dominated  
 56 areas. Permafrost and glacier distributions are shown in medium and dark grey, respectively.  
 57 All times series are smoothed by a 10-yr running mean and indexed to the middle year.

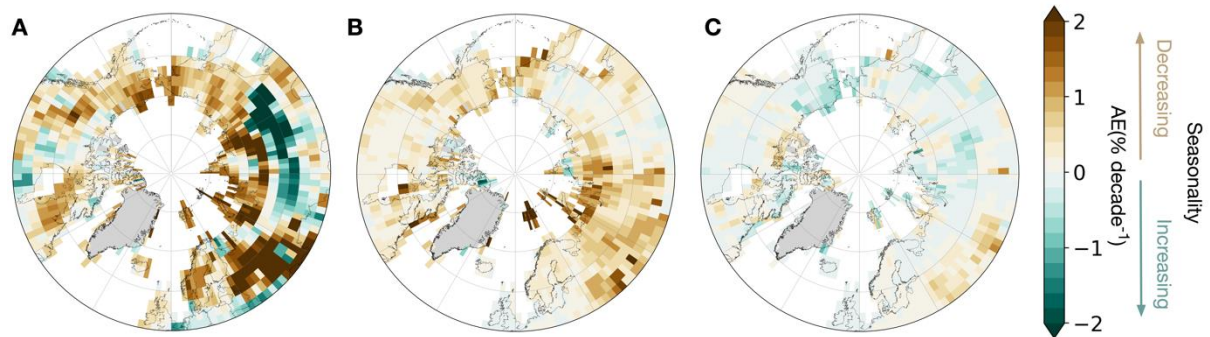


58

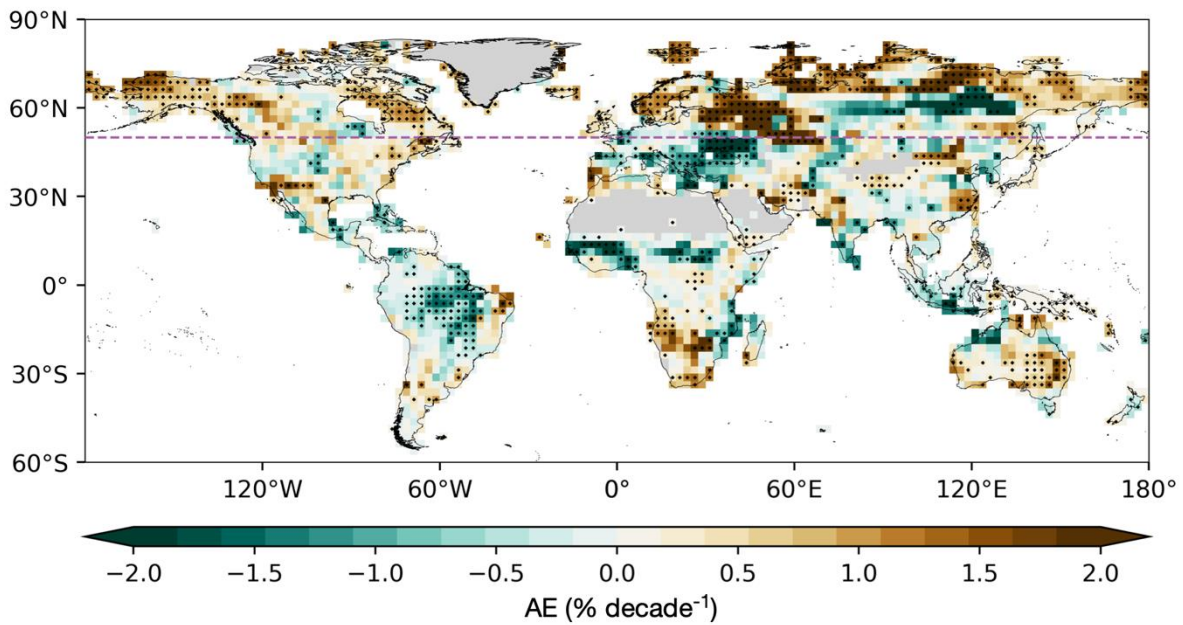
59 **Fig. S7.**

60 Agreement of seasonality trends from 27 GHMs under HIST&HWLU. Fraction of GHMs  
 61 with weakening river flow seasonality at each grid cell. The purple dashed line at 50°N  
 62 highlights the boundary of the northern high latitudes defined in this study. Areas of annual  
 63 precipitation below 100 mm and Greenland are masked in grey.

64

65 **Fig. S8.**

Similar to Fig. 3A-3C in the main text, but with study period replaced with 1970-2019. Note  
66 (A) shows AE trends from CRU-TS, which is one observational runoff reconstruction driven  
67 by the CRUTSv4.04 atmospheric forcing dataset in the G-RUN ENSEMBLE. (B, C)  
68 Simulated changes based on multimodel mean that account for historical water and land use  
69 (HWLU) under either historical radiative forcing (HIST) (B) or pre-industrial control  
70 (Picontrol) (C). Areas with annual precipitation below 100 mm and Greenland are masked in  
71 grey.  
72

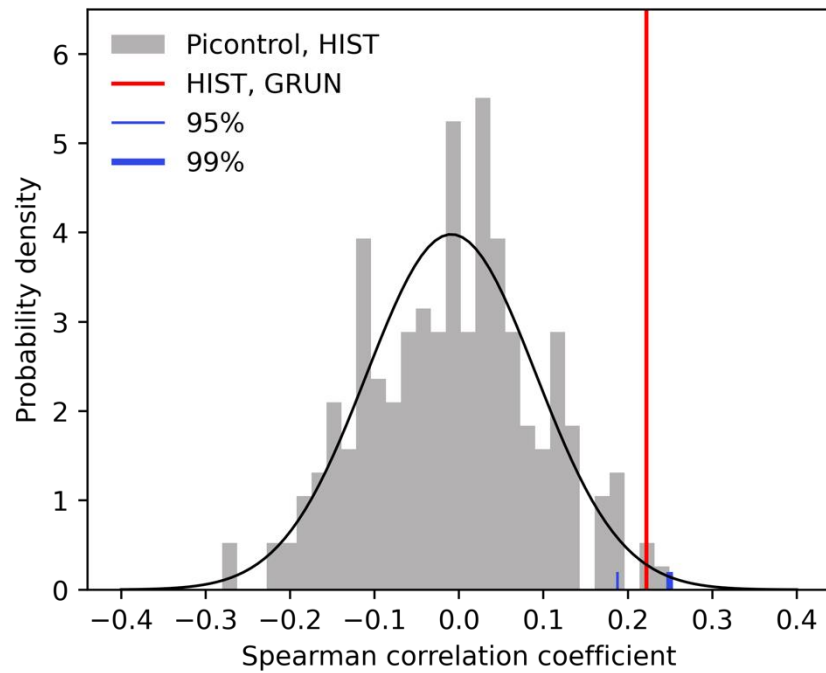


73

74 **Fig. S9.**

75 Observational reconstruction of river flow apportionment entropy (AE) trends (% decade<sup>-1</sup>)  
 76 for the G-RUN ENSEMBLE member driven with CRU-TS in 1970-2019. Black dots indicate  
 77 a trend significance at 0.05. The purple dashed line at 50°N highlights the boundary of the  
 78 northern high latitudes defined in this study. Areas of annual precipitation below 100 mm and  
 79 Greenland are masked in grey.

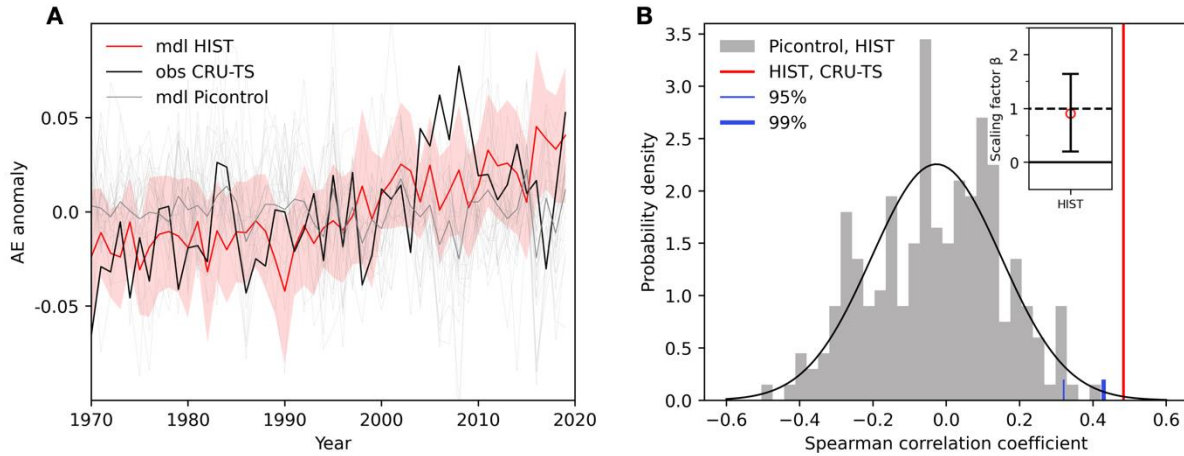
80



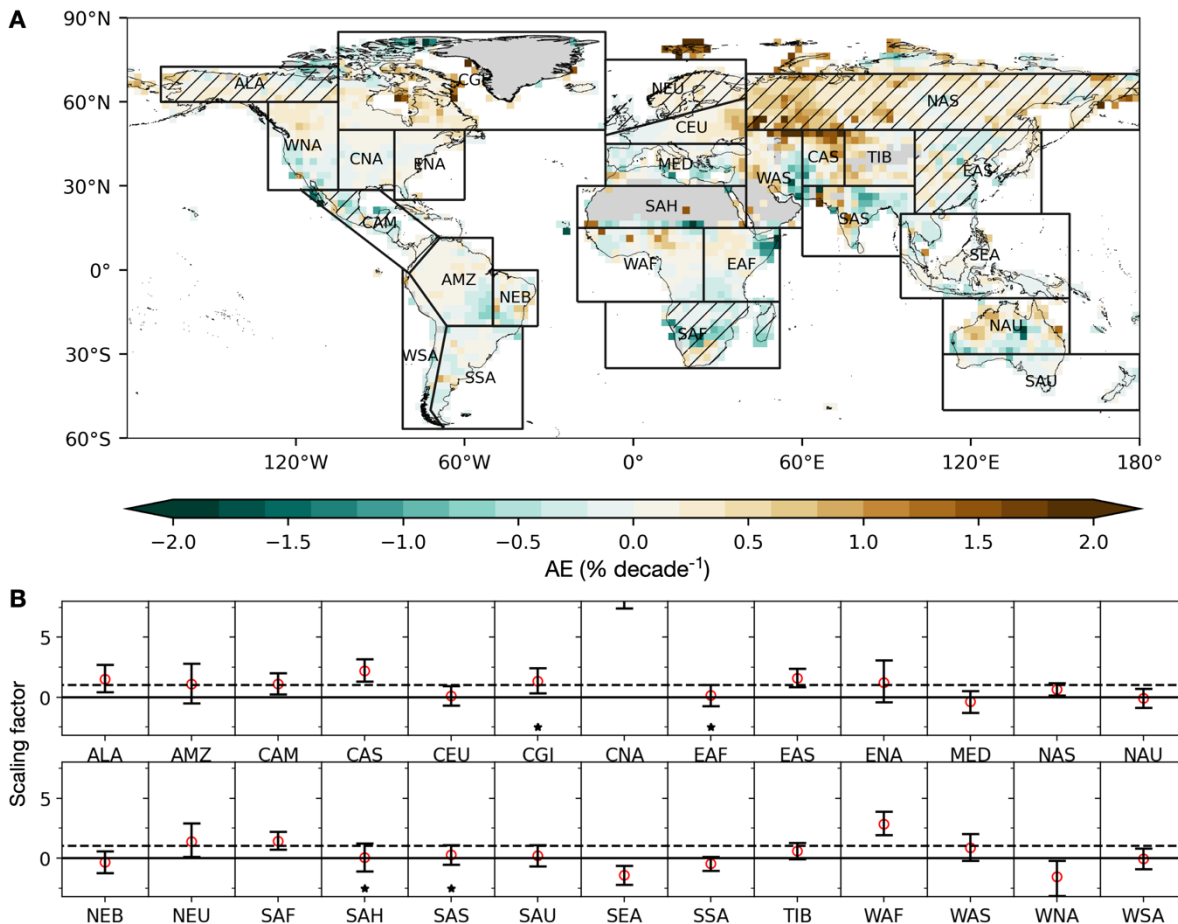
81

**Fig. S10.**

82 Spatial Spearman correlation coefficient of apportionment entropy (AE) trends for 1965-2014  
 83 ( $\% \text{ decade}^{-1}$ ) between the multimodel mean from HIST&HWL and observed changes from  
 84 GRUN ( $\text{corr}_{\text{spatial}}(\text{HIST}, \text{GRUN})$ , red) compared with an empirical distribution of correlation  
 85 coefficients from 216 chunks of Picontrol simulations ( $\text{corr}_{\text{spatial}}(\text{Picontrol}, \text{HIST})$ , grey).  
 86 Vertical blue lines mark the 95% and 99% cumulative probability of an assumed normal  
 87 distribution for the correlations.

89 **Fig. S11.**

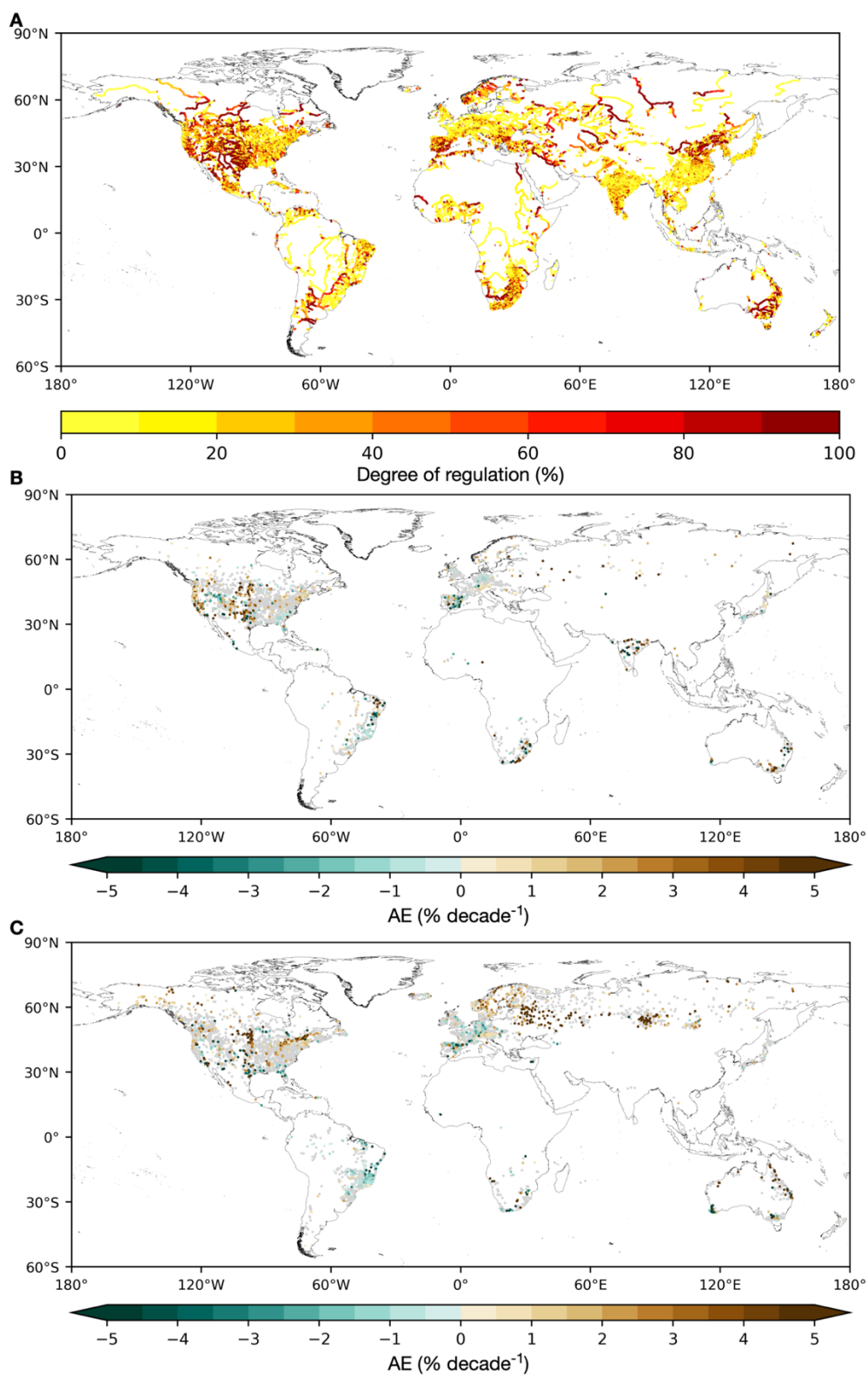
90 Similar to Fig. 3D and 3E in the main text, but with study period replaced with 1970-2019  
 91 and observational runoff replaced with CRU-TS, which is one observational runoff  
 92 reconstruction driven by CRUTSv4.04 atmospheric forcing dataset in the G-RUN  
 93 ENSEMBLE. (A) Global multimodel (mdl) mean time series of apportionment entropy (AE)  
 94 anomalies for HIST&HWLU and Picontrol&HWLU response and CRU-TS observations  
 95 above 50°N. The red spread is ensemble standard deviation of HIST&HWLU, and thin grey  
 96 lines are 27 model results of Picontrol&HWLU. (B) Correlation coefficient of AE anomalies  
 97 between simulations with and without ACC ( $\text{corr}_{\text{temporary}}(\text{Picontrol}, \text{HIST})$ ) or observation-  
 98 based reconstructions ( $\text{corr}_{\text{temporary}}(\text{HIST}, \text{CRU-TS})$ ) across 50°N-90°N. Correlation  
 99 coefficient between the mdl mean from HIST&HWLU simulations and 216 chunks of  
 100 Picontrol simulations with 50-yr segments are shown as an empirical probability density  
 101 function in grey. Vertical blue lines mark the 95% and 99% cumulative probability of an  
 102 assumed normal distribution for the correlations. The inset shows the confidence interval of  
 103 the scaling factor from the optimal fingerprinting method with 0.5-99.5% uncertainty range.  
 104 A signal is detected if the lower confidence bound is above zero (the solid line). The  
 105 amplitude of the mean response is consistent with the observations if the confidence interval  
 106 includes one (the dashed line). The residual consistency test (RCT) passed ( $p >$   
 107 0.1), indicating the consistency between the regression residuals and the model-simulated  
 108 variability.



109

110 **Fig. S12.**

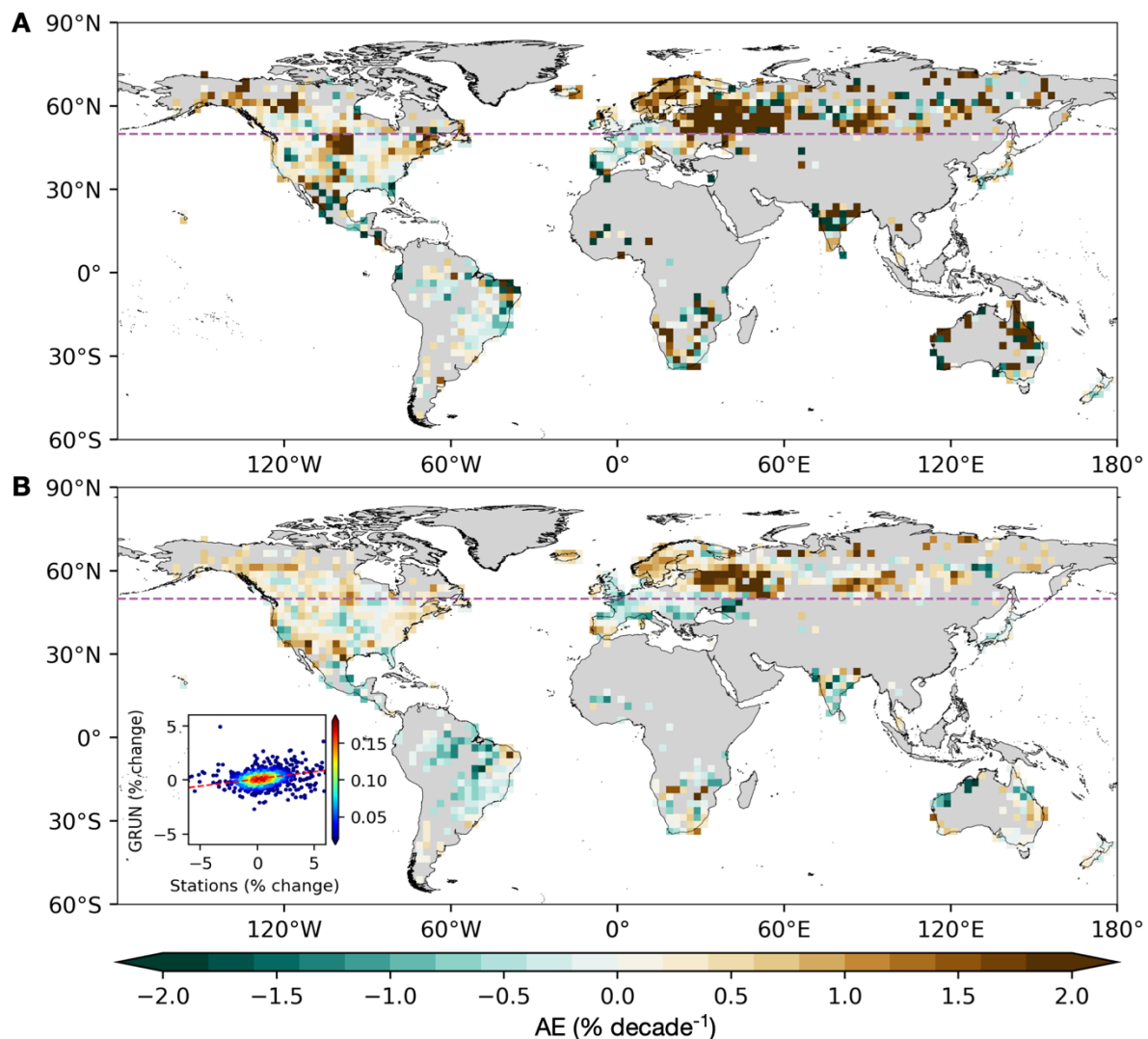
111 Results of the climate change detection and attribution analyses for the Apportionment  
 112 Entropy (AE) of river flow in 26 IPCC SREX regions for 1965-2014. (A) Trends of AE in  
 113 river flow from multimodel mean of global hydrological models ( $\text{percent decade}^{-1}$ ), the same as  
 114 Fig. 3B but at global scale. (B) The scaling factor plots from 26 IPCC SREX refer to 10-90%  
 115 uncertainty ranges from the detection analysis, \* indicates a residual consistency test was not  
 116 passed ( $p < 0.1$ ). Regions with detected signal (lower confidence bound of scaling factor is  
 117 above zero (the solid line)) and attributable to ACC (the confidence interval includes one (the  
 118 dashed line)) are marked with dashes in (A). The ranges of scaling factor are truncated to  
 119 enhance readability of the plot if confidence intervals exceed the ordinate.



120

121 **Fig. S13.**

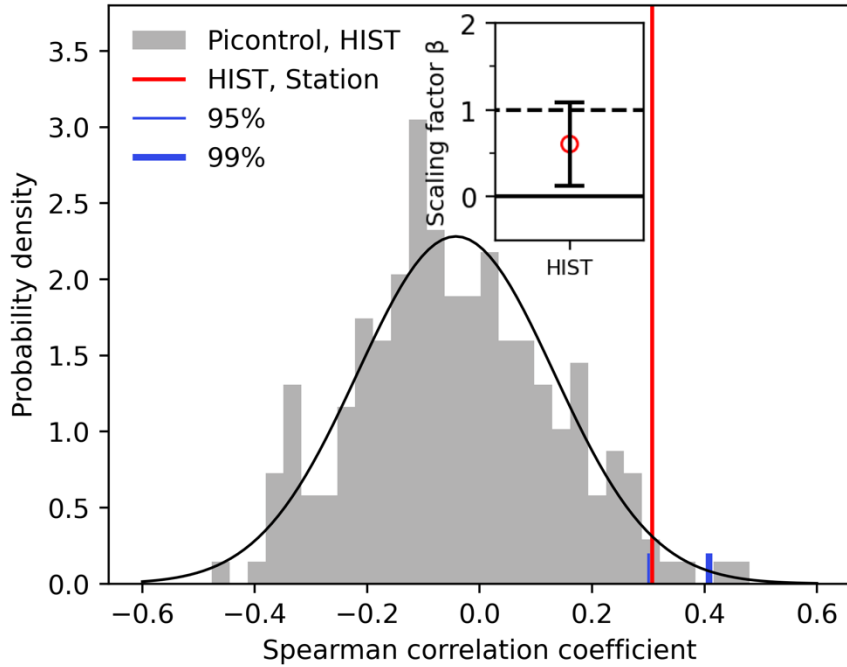
122 River flow seasonality trends represented by apportionment entropy (AE) ( $\% \text{ decade}^{-1}$ ) over  
 123 50 years (1965–2014). (A) Degree of regulation (%) of rivers influenced by reservoirs. (B, C)  
 124 illustrate the AE trends in the stations influenced by reservoirs (3,914) and those unaffected  
 125 by reservoirs (6,150), respectively.



126

127 **Fig. S14.**

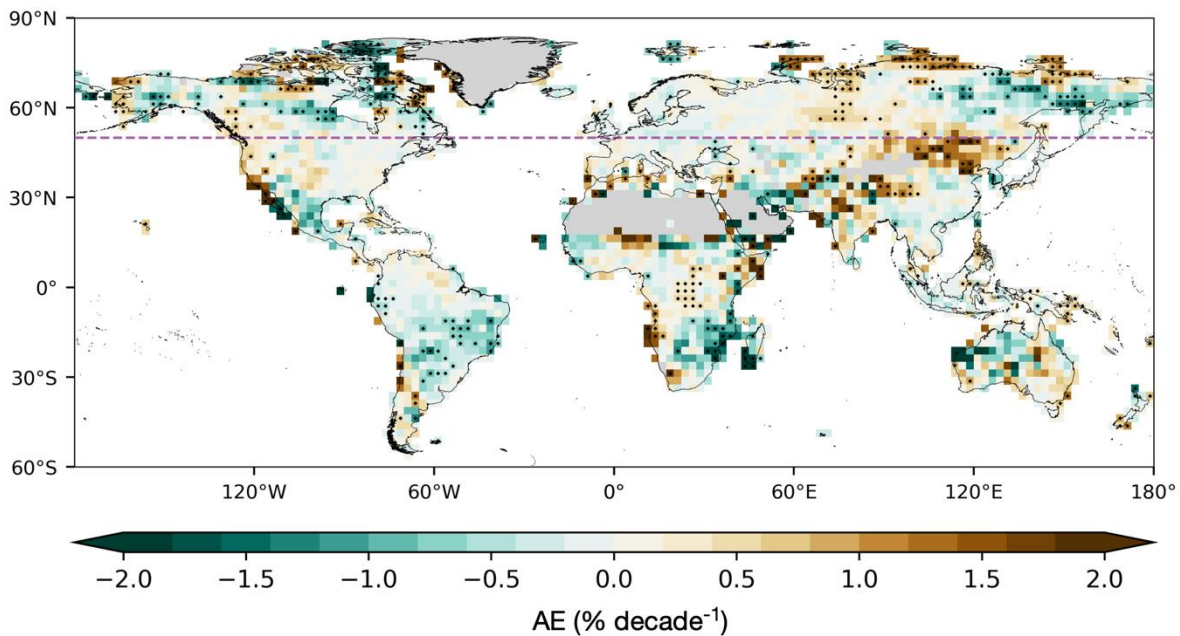
128 Comparison of apportionment entropy (AE) trends from (A) stations and (B) GRUN (%  
 129 decade<sup>-1</sup>). Each grid cell is the median trend for all the stations. Grid cells containing at least  
 130 one station were included. Inset is a scatterplot showing the trends from stations and GRUN  
 131 with linear regression in a red dashed line. Color shows the relative density of data points.  
 132 Stations with trends larger than  $\pm 6\%$  are not showed in the scatterplot, which occupied  $\sim 4\%$   
 133 of 10,120 stations. The purple dashed line at 50°N highlights the boundary of the northern  
 134 high latitudes defined in this study.



135

136 **Fig. S15.**

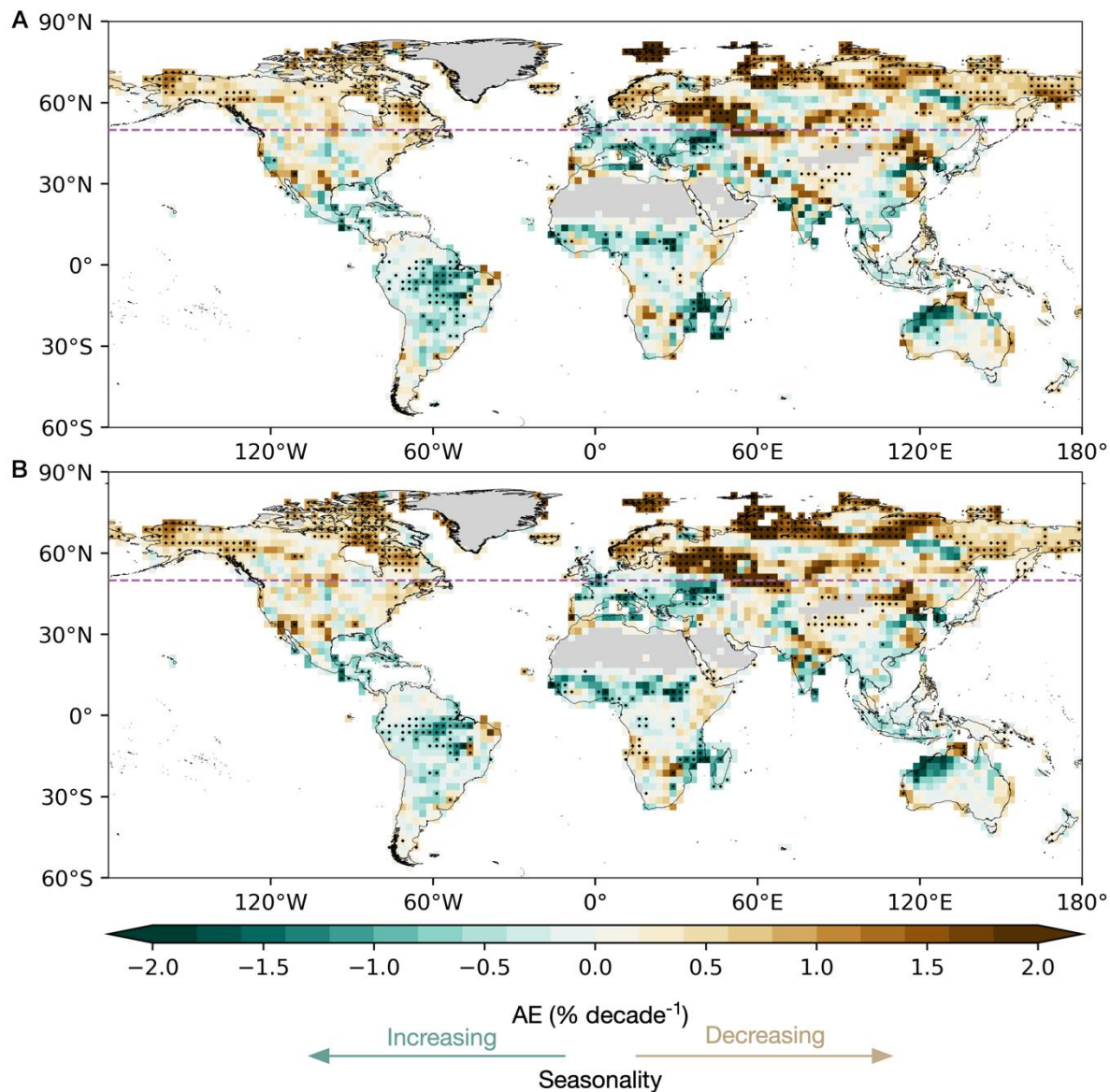
137 Similar to Fig. 3E in the main text, but we replace GRUN with gauged-based observations,  
 138 and the spatial coverage is restricted to grid cells that contain at least one station in the  
 139 northern high latitudes (above 50°N). Correlation coefficient of AE anomalies between  
 140 simulations with and without ACC ( $\text{corr}_{\text{temporary}}(\text{Picontrol}, \text{HIST})$ ) or observation-based  
 141 reconstructions ( $\text{corr}_{\text{temporary}}(\text{HIST}, \text{Station})$ ) across 50°N-90°N. Correlation coefficient  
 142 between the multimodel mean from HIST&HWLU simulations and 216 chunks of Picontrol  
 143 simulations with 50-yr segments are shown as an empirical probability density function in  
 144 grey. Vertical blue lines mark the 95% and 99% cumulative probability of an assumed  
 145 normal distribution for the correlation. The inset shows the confidence interval of the scaling  
 146 factor plot from the optimal fingerprinting method with 10-90% uncertainty range.



147

**Fig. S16.**

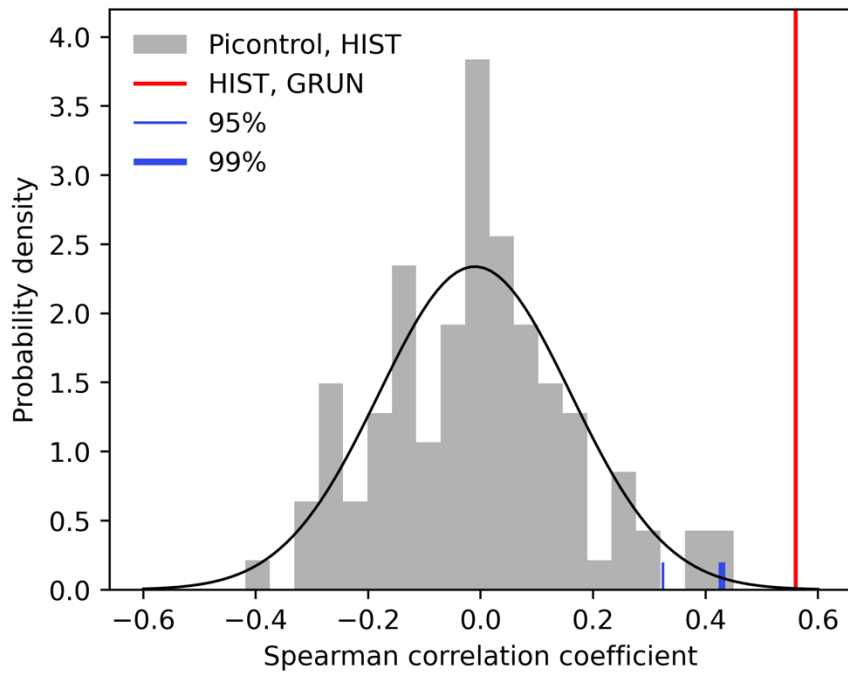
149 Trends in Apportionment Entropy (AE) ( $\% \text{ decade}^{-1}$ ) of precipitation from GPCC in 1965-  
 150 2014. Black dots indicate a trend significance at 0.05. The purple dashed line at 50°N  
 151 highlights the boundary of the northern high latitudes defined in this study. Areas of annual  
 152 precipitation below 100 mm and Greenland are masked in grey.



153

154 **Fig. S17.**

155 Trends in Apportionment Entropy (AE) (% decade<sup>-1</sup>) of (A) river flow from GRUN and (B)  
 156 G-RUN ENSEMBLE, reconstructed from observation in 1965-2014. Black dots indicate a  
 157 trend significance at 0.05. The purple dashed line at 50°N highlights the boundary of the  
 158 northern high latitudes defined in this study. Areas of annual precipitation below 100 mm and  
 159 Greenland are masked in grey.



160

161 **Fig. S18.**

162 Similar to Fig. 3E in the main text, but with Picontrol simulations restricted in  
 163 Picontrol&HWLU. Correlation coefficient of AE anomalies between simulations with and  
 164 without ACC ( $\text{corr}_{\text{temporary}}(\text{Picontrol}, \text{HIST})$ ) or observation-based reconstructions  
 165 ( $\text{corr}_{\text{temporary}}(\text{HIST}, \text{GRUN})$ ) across 50°N-90°N. Correlation coefficient between the  
 166 multimodel mean from HIST&HWLU simulations and 108 chunks of Picontrol simulations  
 167 with 50-yr segments are shown as an empirical probability density function in grey. Vertical  
 168 blue lines mark the 95% and 99% cumulative probability of an assumed normal distribution  
 169 for the correlation.

170      **Table S1.** Spearman's rank correlation coefficients between the river flow AE with  
 171      precipitation AE, soil moisture, snow fraction, and air temperature in the nine hotspots of Fig.  
 172      S6. \* indicates the trends are significant ( $p < 0.05$ ).

<b>Regions</b>	<b>precipitation AE</b>	<b>soil moisture</b>	<b>snow fraction</b>	<b>air temperature</b>
<b>N.NA</b>	-0.57*	-0.58*	-0.8*	0.9*
<b>N.EU</b>	0.37*	0.01	-0.87*	0.86*
<b>W.RU</b>	-0.78*	-0.15	-0.63*	-0.07
<b>Alps</b>	0.06	-0.77*	-0.78*	0.86*
<b>S.SI</b>	-0.04	-0.58*	-0.67*	0.55*
<b>Pacific NW.</b>	0.65*	-0.17	-0.11	0.32*
<b>U. Midwest</b>	-0.2	0.37*	-0.89*	0.83*
<b>NE.</b>	0.04	-0.47*	-0.55*	0.7*
<b>S. BR</b>	0.93*	0.27		-0.64*

173

**Table S2.** Ensemble simulations and hydrology models included in our analysis.

		climate scenario					
		Pre-industrial control (Picontrol)			Historical (HIST)		RCP6.0
	Simulation period	1661-1860	1861-2005	2006-2099	1861-2005	2006-2099	
GHM/LSM	social & economy scenarios GCM	1860soc	histsoc	2005soc	2005soc	histsoc	2005soc
CLM45	GFDL-ESM2M	Y		Y	Y		Y
	HadGEM2-ES	Y		Y	Y		Y
	IPSL-CM5A-LR	Y		Y	Y		Y
	MIROC5	Y		Y	Y		Y
H08	GFDL-ESM2M	Y	Y		Y	Y	
	HadGEM2-ES	Y	Y		Y	Y	
	IPSL-CM5A-LR	Y	Y		Y	Y	
	MIROC5	Y	Y		Y	Y	
LPJmL	GFDL-ESM2M	Y	Y		Y	Y	
	HadGEM2-ES	Y	Y		Y	Y	
	IPSL-CM5A-LR	Y	Y		Y	Y	
	MIROC5	Y	Y		Y	Y	
MATSIRO	GFDL-ESM2M	Y	Y		Y	Y	
	HadGEM2-ES	Y	Y		Y	Y	
	IPSL-CM5A-LR	Y	Y		Y	Y	
	MIROC5	Y	Y		Y	Y	
MPI-HM	GFDL-ESM2M	Y	Y		Y	Y	
	IPSL-CM5A-LR	Y	Y		Y	Y	
	MIROC5	Y	Y		Y	Y	
PCR-GLOBWB	GFDL-ESM2M	Y	Y		Y	Y	
	HadGEM2-ES	Y	Y		Y	Y	
	IPSL-CM5A-LR	Y	Y		Y	Y	
	MIROC5	Y	Y		Y	Y	
WaterGAP2	GFDL-ESM2M	Y	Y		Y	Y	
	HadGEM2-ES	Y	Y		Y	Y	
	IPSL-CM5A-LR	Y	Y		Y	Y	
	MIROC5	Y	Y		Y	Y	

**Table S3.** Monthly streamflow databases included in the analysis during 1970-2019.

Database	Spatial coverage	Data access information
Global Runoff Data Centre (GRDC) (52)	Global	<a href="https://www.bafg.de/GRDC/">https://www.bafg.de/GRDC/</a>
United States Geological Survey water data (USGS)	USA	<a href="https://waterdata.usgs.gov/nwis">https://waterdata.usgs.gov/nwis</a>
Canada National Water Data Archive (HYDAT)	Canada	<a href="https://wateroffice.ec.gc.ca/">https://wateroffice.ec.gc.ca/</a>
Brazil National Water Agency (ANA)	Brazil	<a href="http://hidroweb.ana.gov.br/">http://hidroweb.ana.gov.br/</a>
African Database of Hydrometric Indices (ADHI) (68)	Africa	<a href="https://doi.org/10.23708/LXGXQ9">https://doi.org/10.23708/LXGXQ9</a>

## References and Notes

1. P. Wu, N. Christidis, P. Stott, Anthropogenic impact on Earth's hydrological cycle. *Nat. Clim. Chang.* **3**, 807–810 (2013). [doi:10.1038/nclimate1932](https://doi.org/10.1038/nclimate1932)
2. C. J. Vörösmarty, P. Green, J. Salisbury, R. B. Lammers, Global water resources: Vulnerability from climate change and population growth. *Science* **289**, 284–288 (2000). [doi:10.1126/science.289.5477.284](https://doi.org/10.1126/science.289.5477.284) [Medline](#)
3. P. C. D. Milly, K. A. Dunne, A. V. Vecchia, Global pattern of trends in streamflow and water availability in a changing climate. *Nature* **438**, 347–350 (2005). [doi:10.1038/nature04312](https://doi.org/10.1038/nature04312) [Medline](#)
4. N. K. Singh, N. B. Basu, The human factor in seasonal streamflows across natural and managed watersheds of North America. *Nat. Sustain.* **5**, 397–405 (2022). [doi:10.1038/s41893-022-00848-1](https://doi.org/10.1038/s41893-022-00848-1)
5. G. Blöschl, J. Hall, A. Viglione, R. A. P. Perdigão, J. Parajka, B. Merz, D. Lun, B. Arheimer, G. T. Aronica, A. Bilibashi, M. Boháč, O. Bonacci, M. Borga, I. Čanjevac, A. Castellarin, G. B. Chirico, P. Claps, N. Frolova, D. Ganora, L. Gorbachova, A. Gül, J. Hannaford, S. Harrigan, M. Kireeva, A. Kiss, T. R. Kjeldsen, S. Kohnová, J. J. Koskela, O. Ledvinka, N. Macdonald, M. Mavrova-Guirguinova, L. Mediero, R. Merz, P. Molnar, A. Montanari, C. Murphy, M. Osuch, V. Ovcharuk, I. Radevski, J. L. Salinas, E. Sauquet, M. Šraj, J. Szolgay, E. Volpi, D. Wilson, K. Zaimi, N. Živković, Changing climate both increases and decreases European river floods. *Nature* **573**, 108–111 (2019). [doi:10.1038/s41586-019-1495-6](https://doi.org/10.1038/s41586-019-1495-6) [Medline](#)
6. G. Blöschl, J. Hall, J. Parajka, R. A. P. Perdigão, B. Merz, B. Arheimer, G. T. Aronica, A. Bilibashi, O. Bonacci, M. Borga, I. Čanjevac, A. Castellarin, G. B. Chirico, P. Claps, K. Fiala, N. Frolova, L. Gorbachova, A. Gül, J. Hannaford, S. Harrigan, M. Kireeva, A. Kiss, T. R. Kjeldsen, S. Kohnová, J. J. Koskela, O. Ledvinka, N. Macdonald, M. Mavrova-Guirguinova, L. Mediero, R. Merz, P. Molnar, A. Montanari, C. Murphy, M. Osuch, V. Ovcharuk, I. Radevski, M. Rogger, J. L. Salinas, E. Sauquet, M. Šraj, J. Szolgay, A. Viglione, E. Volpi, D. Wilson, K. Zaimi, N. Živković, Changing climate shifts timing of European floods. *Science* **357**, 588–590 (2017). [doi:10.1126/science.aan2506](https://doi.org/10.1126/science.aan2506) [Medline](#)
7. M. Dynesius, C. Nilsson, Fragmentation and flow regulation of river systems in the northern third of the world. *Science* **266**, 753–762 (1994). [doi:10.1126/science.266.5186.753](https://doi.org/10.1126/science.266.5186.753) [Medline](#)
8. M. Palmer, A. Ruhi, Linkages between flow regime, biota, and ecosystem processes: Implications for river restoration. *Science* **365**, eaaw2087 (2019). [doi:10.1126/science.aaw2087](https://doi.org/10.1126/science.aaw2087) [Medline](#)
9. T. P. Barnett, J. C. Adam, D. P. Lettenmaier, Potential impacts of a warming climate on water availability in snow-dominated regions. *Nature* **438**, 303–309 (2005). [doi:10.1038/nature04141](https://doi.org/10.1038/nature04141) [Medline](#)
10. J. D. Tonkin, D. M. Merritt, J. D. Olden, L. V. Reynolds, D. A. Lytle, Flow regime alteration degrades ecological networks in riparian ecosystems. *Nat. Ecol. Evol.* **2**, 86–93 (2018). [doi:10.1038/s41559-017-0379-0](https://doi.org/10.1038/s41559-017-0379-0) [Medline](#)
11. S. B. Rood, J. Pan, K. M. Gill, C. G. Franks, G. M. Samuelson, A. Shepherd, Declining summer flows of Rocky Mountain rivers: Changing seasonal hydrology and probable impacts on floodplain forests. *J. Hydrol. (Amst.)* **349**, 397–410 (2008). [doi:10.1016/j.jhydrol.2007.11.012](https://doi.org/10.1016/j.jhydrol.2007.11.012)

12. H. L. Bateman, D. M. Merritt, Complex riparian habitats predict reptile and amphibian diversity. *Glob. Ecol. Conserv.* **22**, e00957 (2020). [doi:10.1016/j.gecco.2020.e00957](https://doi.org/10.1016/j.gecco.2020.e00957)
13. C. Wasko, R. Nathan, M. C. Peel, Trends in Global Flood and Streamflow Timing Based on Local Water Year. *Water Resour. Res.* **56**, e2020WR027233 (2020). [doi:10.1029/2020WR027233](https://doi.org/10.1029/2020WR027233)
14. S. Eisner, M. Flörke, A. Chamorro, P. Daggupati, C. Donnelly, J. Huang, Y. Hundecha, H. Koch, A. Kalugin, I. Krylenko, V. Mishra, M. Piniewski, L. Samaniego, O. Seidou, M. Wallner, V. Krysanova, An ensemble analysis of climate change impacts on streamflow seasonality across 11 large river basins. *Clim. Change* **141**, 401–417 (2017). [doi:10.1007/s10584-016-1844-5](https://doi.org/10.1007/s10584-016-1844-5)
15. K. Marvel, B. I. Cook, C. Bonfils, J. E. Smerdon, A. P. Williams, H. Liu, Projected Changes to Hydroclimate Seasonality in the Continental United States. *Earth's Futur.* **9**, e2021EF002019 (2021). [doi:10.1029/2021EF002019](https://doi.org/10.1029/2021EF002019)
16. T. P. Barnett, D. W. Pierce, H. G. Hidalgo, C. Bonfils, B. D. Santer, T. Das, G. Bala, A. W. Wood, T. Nozawa, A. A. Mirin, D. R. Cayan, M. D. Dettinger, Human-induced changes in the hydrology of the western United States. *Science* **319**, 1080–1083 (2008). [doi:10.1126/science.1152538](https://doi.org/10.1126/science.1152538) [Medline](#)
17. L. Gudmundsson, S. I. Seneviratne, X. Zhang, Anthropogenic climate change detected in European renewable freshwater resources. *Nat. Clim. Chang.* **7**, 813–816 (2017). [doi:10.1038/nclimate3416](https://doi.org/10.1038/nclimate3416)
18. H. X. Do, L. Gudmundsson, M. Leonard, S. Westra, The Global Streamflow Indices and Metadata Archive (GSIM)-Part 1: The production of a daily streamflow archive and metadata. *Earth Syst. Sci. Data* **10**, 765–785 (2018). [doi:10.5194/essd-10-765-2018](https://doi.org/10.5194/essd-10-765-2018)
19. G. Ghiggi, V. Humphrey, S. I. Seneviratne, L. Gudmundsson, GRUN: An observation-based global gridded runoff dataset from 1902 to 2014. *Earth Syst. Sci. Data* **11**, 1655–1674 (2019). [doi:10.5194/essd-11-1655-2019](https://doi.org/10.5194/essd-11-1655-2019)
20. K. Frieler, S. Lange, F. Piontek, C. P. O. Reyer, J. Schewe, L. Warszawski, F. Zhao, L. Chini, S. Denvil, K. Emanuel, T. Geiger, K. Halladay, G. Hurtt, M. Mengel, D. Murakami, S. Ostberg, A. Popp, R. Riva, M. Stevanovic, T. Suzuki, J. Volkholz, E. Burke, P. Ciais, K. Ebi, T. D. Eddy, J. Elliott, E. Galbraith, S. N. Gosling, F. Hattermann, T. Hickler, J. Hinkel, C. Hof, V. Huber, J. Jägermeyr, V. Krysanova, R. Marcé, H. Müller Schmied, I. Mouratiadou, D. Pierson, D. P. Tittensor, R. Vautard, M. van Vliet, M. F. Biber, R. A. Betts, B. L. Bodirsky, D. Deryng, S. Frolking, C. D. Jones, H. K. Lotze, H. Lotze-Campen, R. Sahajpal, K. Thonicke, H. Tian, Y. Yamagata, Assessing the impacts of 1.5°C global warming - simulation protocol of the Inter-Sectoral Impact Model Intercomparison Project (ISIMIP2b). *Geosci. Model Dev.* **10**, 4321–4345 (2017). [doi:10.5194/gmd-10-4321-2017](https://doi.org/10.5194/gmd-10-4321-2017)
21. X. Feng, A. Porporato, I. Rodriguez-Iturbe, Changes in rainfall seasonality in the tropics. *Nat. Clim. Chang.* **3**, 811–815 (2013). [doi:10.1038/nclimate1907](https://doi.org/10.1038/nclimate1907)
22. G. Konapala, A. K. Mishra, Y. Wada, M. E. Mann, Climate change will affect global water availability through compounding changes in seasonal precipitation and evaporation. *Nat. Commun.* **11**, 3044 (2020). [doi:10.1038/s41467-020-16757-w](https://doi.org/10.1038/s41467-020-16757-w) [Medline](#)
23. E. N. Dethier, S. L. Sartain, C. E. Renshaw, F. J. Magilligan, Spatially coherent regional changes in seasonal extreme streamflow events in the United States and Canada since 1950. *Sci. Adv.* **6**, eaba5939 (2020). [doi:10.1126/sciadv.aba5939](https://doi.org/10.1126/sciadv.aba5939) [Medline](#)

24. M. R. Viola, C. R. de Mello, S. C. Chou, S. N. Yanagi, J. L. Gomes, Assessing climate change impacts on Upper Grande River Basin hydrology, Southeast Brazil. *Int. J. Climatol.* **35**, 1054–1068 (2015). [doi:10.1002/joc.4038](https://doi.org/10.1002/joc.4038)
25. D. Bartiko, D. Y. Oliveira, N. B. Bonumá, P. L. B. Chaffé, Spatial and seasonal patterns of flood change across Brazil. *Hydrol. Sci. J.* **64**, 1071–1079 (2019). [doi:10.1080/02626667.2019.1619081](https://doi.org/10.1080/02626667.2019.1619081)
26. V. Virkki, E. Alanärä, M. Porkka, L. Ahopelto, T. Gleeson, C. Mohan, L. Wang-Erlandsson, M. Flörke, D. Gerten, S. N. Gosling, N. Hanasaki, H. Müller Schmied, N. Wanders, M. Kummu, Globally widespread and increasing violations of environmental flow envelopes. *Hydrol. Earth Syst. Sci.* **26**, 3315–3336 (2022). [doi:10.5194/hess-26-3315-2022](https://doi.org/10.5194/hess-26-3315-2022)
27. X. Lian, S. Piao, L. Z. X. Li, Y. Li, C. Huntingford, P. Ciais, A. Cescatti, I. A. Janssens, J. Peñuelas, W. Buermann, A. Chen, X. Li, R. B. Myneni, X. Wang, Y. Wang, Y. Yang, Z. Zeng, Y. Zhang, T. R. McVicar, Summer soil drying exacerbated by earlier spring greening of northern vegetation. *Sci. Adv.* **6**, eaax0255 (2020). [doi:10.1126/sciadv.aax0255](https://doi.org/10.1126/sciadv.aax0255) [Medline](#)
28. E. Gautier, T. Dépret, F. Costard, C. Virmoux, A. Fedorov, D. Grancher, P. Konstantinov, D. Brunstein, Going with the flow: Hydrologic response of middle Lena River (Siberia) to the climate variability and change. *J. Hydrol. (Amst.)* **557**, 475–488 (2018). [doi:10.1016/j.jhydrol.2017.12.034](https://doi.org/10.1016/j.jhydrol.2017.12.034)
29. V. B. P. Chagas, P. L. B. Chaffé, G. Blöschl, Process Controls on Flood Seasonality in Brazil. *Geophys. Res. Lett.* **49**, e2021GL096754 (2022). [doi:10.1029/2021GL096754](https://doi.org/10.1029/2021GL096754)
30. P. W. Mote, S. Li, D. P. Lettenmaier, M. Xiao, R. Engel, Dramatic declines in snowpack in the western US. *NPJ Clim. Atmos. Sci.* **1**, 2 (2018). [doi:10.1038/s41612-018-0012-1](https://doi.org/10.1038/s41612-018-0012-1)
31. D. Lee, P. J. Ward, P. Block, Identification of symmetric and asymmetric responses in seasonal streamflow globally to ENSO phase. *Environ. Res. Lett.* **13**, 044031 (2018). [doi:10.1088/1748-9326/aab4ca](https://doi.org/10.1088/1748-9326/aab4ca)
32. R. S. Padrón, L. Gudmundsson, B. Decharme, A. Ducharne, D. M. Lawrence, J. Mao, D. Peano, G. Krinner, H. Kim, S. I. Seneviratne, Observed changes in dry-season water availability attributed to human-induced climate change. *Nat. Geosci.* **13**, 477–481 (2020). [doi:10.1038/s41561-020-0594-1](https://doi.org/10.1038/s41561-020-0594-1)
33. L. Grant, I. Vanderkelen, L. Gudmundsson, Z. Tan, M. Perroud, V. M. Stepanenko, A. V. Debolskiy, B. Droppers, A. B. G. Janssen, R. I. Woolway, M. Choulga, G. Balsamo, G. Kirillin, J. Schewe, F. Zhao, I. V. del Valle, M. Golub, D. Pierson, R. Marcé, S. I. Seneviratne, W. Thiery, Attribution of global lake systems change to anthropogenic forcing. *Nat. Geosci.* **14**, 849–854 (2021). [doi:10.1038/s41561-021-00833-x](https://doi.org/10.1038/s41561-021-00833-x)
34. A. Ribes, S. Planton, L. Terray, Application of regularised optimal fingerprinting to attribution. Part I: Method, properties and idealised analysis. *Clim. Dyn.* **41**, 2817–2836 (2013). [doi:10.1007/s00382-013-1735-7](https://doi.org/10.1007/s00382-013-1735-7)
35. B. Arheimer, C. Donnelly, G. Lindström, Regulation of snow-fed rivers affects flow regimes more than climate change. *Nat. Commun.* **8**, 62 (2017). [doi:10.1038/s41467-017-00092-8](https://doi.org/10.1038/s41467-017-00092-8) [Medline](#)
36. L. Gudmundsson, J. Boulange, H. X. Do, S. N. Gosling, M. G. Grillakis, A. G. Koutroulis, M. Leonard, J. Liu, H. Müller Schmied, L. Papadimitriou, Y. Pokhrel, S. I. Seneviratne, Y. Satoh, W. Thiery, S. Westra, X. Zhang, F. Zhao, Globally observed

- trends in mean and extreme river flow attributed to climate change. *Science* **371**, 1159–1162 (2021). [doi:10.1126/science.aba3996](https://doi.org/10.1126/science.aba3996) [Medline](#)
37. IPCC, “Anthropogenic and Natural Radiative Forcing” in *Climate Change 2013: The Physical Science Basis* (Cambridge Univ. Press, 2013), pp. 659–740.
38. C. E. Iles, G. C. Hegerl, Systematic change in global patterns of streamflow following volcanic eruptions. *Nat. Geosci.* **8**, 838–842 (2015). [doi:10.1038/ngeo2545](https://doi.org/10.1038/ngeo2545) [Medline](#)
39. M. Huss, R. Hock, Global-scale hydrological response to future glacier mass loss. *Nat. Clim. Chang.* **8**, 135–140 (2018). [doi:10.1038/s41558-017-0049-x](https://doi.org/10.1038/s41558-017-0049-x)
40. L. Gudmundsson, J. Kirchner, A. Gädeke, J. Noetzli, B. K. Biskaborn, Attributing observed permafrost warming in the northern hemisphere to anthropogenic climate change. *Environ. Res. Lett.* **17**, 095014 (2022). [doi:10.1088/1748-9326/ac8ec2](https://doi.org/10.1088/1748-9326/ac8ec2)
41. W. R. Berghuijs, R. A. Woods, M. Hrachowitz, A precipitation shift from snow towards rain leads to a decrease in streamflow. *Nat. Clim. Chang.* **4**, 583–586 (2014). [doi:10.1038/nclimate2246](https://doi.org/10.1038/nclimate2246)
42. M. G. Floriancic, W. R. Berghuijs, P. Molnar, J. W. Kirchner, Seasonality and Drivers of Low Flows Across Europe and the United States. *Water Resour. Res.* **57**, e2019WR026928 (2021). [doi:10.1029/2019WR026928](https://doi.org/10.1029/2019WR026928)
43. M. Mudelsee, M. Börngen, G. Tetzlaff, U. Grünwald, No upward trends in the occurrence of extreme floods in central Europe. *Nature* **425**, 166–169 (2003). [doi:10.1038/nature01928](https://doi.org/10.1038/nature01928) [Medline](#)
44. J. D. Hunt, E. Byers, Y. Wada, S. Parkinson, D. E. H. J. Gernaat, S. Langan, D. P. van Vuuren, K. Riahi, Global resource potential of seasonal pumped hydropower storage for energy and water storage. *Nat. Commun.* **11**, 947 (2020). [doi:10.1038/s41467-020-14555-y](https://doi.org/10.1038/s41467-020-14555-y) [Medline](#)
45. N. L. Poff, J. D. Olden, D. M. Merritt, D. M. Pepin, Homogenization of regional river dynamics by dams and global biodiversity implications. *Proc. Natl. Acad. Sci. U.S.A.* **104**, 5732–5737 (2007). [doi:10.1073/pnas.0609812104](https://doi.org/10.1073/pnas.0609812104) [Medline](#)
46. L. Gudmundsson, H. X. Do, M. Leonard, S. Westra, The Global Streamflow Indices and Metadata Archive (GSIM) - Part 2: Time Series Indices and Homogeneity Assessment, PANGAEA (2018); <https://doi.org/10.1594/PANGAEA.887470>.
47. G. Ghiggi, L. Gudmundsson, V. Humphrey, G-RUN: Global Runoff Reconstruction, Figshare, version 2, (2019); <https://doi.org/10.6084/m9.figshare.9228176.v2>.
48. U. Schneider, S. Hänsel, P. Finger, E. Rustemeier, M. Ziese, GPCC Full Data Monthly Product Version, 2022 at 2.5°: Monthly Land-Surface Precipitation from Rain-Gauges built on GTS-based and Historical Data, Deutscher Wetterdienst, (2022); [https://doi.org/10.5676/DWD\\_GPCC/FD\\_M\\_V2022\\_250](https://doi.org/10.5676/DWD_GPCC/FD_M_V2022_250).
49. M. Cucchi, G. P. Weedon, A. Amici, N. Bellouin, S. Lange, H. Müller Schmied, H. Hersbach, C. Cagnazzo, C. Buontempo, Near surface meteorological variables from 1979 to 2019 derived from bias-corrected reanalysis, Copernicus Climate Change Service (C3S) Climate Data Store (CDS), version 2.1, (2020); <https://doi.org/10.24381/cds.20d54e34>.
50. J. Muñoz Sabater, ERA5-Land hourly data from 1950 to present, Copernicus Climate Change Service (C3S) Climate Data Store (CDS), (2019); <https://doi.org/10.24381/cds.68d2bb30>.

51. L. Gudmundsson, M. Leonard, H. X. Do, S. Westra, S. I. Seneviratne, Observed Trends in Global Indicators of Mean and Extreme Streamflow. *Geophys. Res. Lett.* **46**, 756–766 (2019). [doi:10.1029/2018GL079725](https://doi.org/10.1029/2018GL079725)
52. Global Runoff Data Centre, In-situ river discharge data, World Meteorological Organization (2015); [https://www.bafg.de/GRDC/EN/Home/homepage\\_node.html](https://www.bafg.de/GRDC/EN/Home/homepage_node.html).
53. G. Ghiggi, V. Humphrey, S. I. Seneviratne, L. Gudmundsson, G-RUN ENSEMBLE: A Multi-Forcing Observation-Based Global Runoff Reanalysis. *Water Resour. Res.* **57**, e2020WR028787 (2021). [doi:10.1029/2020WR028787](https://doi.org/10.1029/2020WR028787)
54. B. Lehner, K. Verdin, A. Jarvis, New global hydrography derived from spaceborne elevation data. *Eos* **89**, 93–94 (2008). [doi:10.1029/2008EO100001](https://doi.org/10.1029/2008EO100001)
55. G. Grill, B. Lehner, M. Thieme, B. Geenen, D. Tickner, F. Antonelli, S. Babu, P. Borrelli, L. Cheng, H. Crochetiere, H. Ehalt Macedo, R. Filgueiras, M. Goichot, J. Higgins, Z. Hogan, B. Lip, M. E. McClain, J. Meng, M. Mulligan, C. Nilsson, J. D. Olden, J. J. Opperman, P. Petry, C. Reidy Liermann, L. Sáenz, S. Salinas-Rodríguez, P. Schelle, R. J. P. Schmitt, J. Snider, F. Tan, K. Tockner, P. H. Valdujo, A. van Soesbergen, C. Zarfl, Mapping the world's free-flowing rivers. *Nature* **569**, 215–221 (2019). [doi:10.1038/s41586-019-1111-9](https://doi.org/10.1038/s41586-019-1111-9) [Medline](#)
56. M. Cucchi, G. P. Weedon, A. Amici, N. Bellouin, S. Lange, H. Müller Schmied, H. Hersbach, C. Buontempo, WFDE5: Bias-adjusted ERA5 reanalysis data for impact studies. *Earth Syst. Sci. Data* **12**, 2097–2120 (2020). [doi:10.5194/essd-12-2097-2020](https://doi.org/10.5194/essd-12-2097-2020)
57. H. Hersbach, B. Bell, P. Berrisford, S. Hirahara, A. Horányi, J. Muñoz-Sabater, J. Nicolas, C. Peubey, R. Radu, D. Schepers, A. Simmons, C. Soci, S. Abdalla, X. Abellan, G. Balsamo, P. Bechtold, G. Biavati, J. Bidlot, M. Bonavita, G. De Chiara, P. Dahlgren, D. Dee, M. Diamantakis, R. Dragani, J. Flemming, R. Forbes, M. Fuentes, A. Geer, L. Haimberger, S. Healy, R. J. Hogan, E. Hólm, M. Janisková, S. Keeley, P. Laloyaux, P. Lopez, C. Lupu, G. Radnoti, P. de Rosnay, I. Rozum, F. Vamborg, S. Villaume, J. N. Thépaut, The ERA5 global reanalysis. *Q. J. R. Meteorol. Soc.* **146**, 1999–2049 (2020). [doi:10.1002/qj.3803](https://doi.org/10.1002/qj.3803)
58. A. Becker, P. Finger, A. Meyer-Christoffer, B. Rudolf, K. Schamm, U. Schneider, M. Ziese, A description of the global land-surface precipitation data products of the Global Precipitation Climatology Centre with sample applications including centennial (trend) analysis from 1901-present. *Earth Syst. Sci. Data* **5**, 71–99 (2013). [doi:10.5194/essd-5-71-2013](https://doi.org/10.5194/essd-5-71-2013)
59. T. J. Osborn, P. D. Jones, D. H. Lister, C. P. Morice, I. R. Simpson, J. P. Winn, E. Hogan, I. C. Harris, Land Surface Air Temperature Variations Across the Globe Updated to 2019: The CRUTEM5 Data Set. *J. Geophys. Res. Atmos.* **126**, e2019JD032352 (2021). [doi:10.1029/2019JD032352](https://doi.org/10.1029/2019JD032352)
60. J. Brown, O. Ferrians, J. A. Heginbottom, E. Melnikov, *Circum-Arctic Map of Permafrost and Ground-Ice Conditions, Version 2* (National Snow and Ice Data Center, 2002).
61. W. T. Pfeffer, A. A. Arendt, A. Bliss, T. Bolch, J. G. Cogley, A. S. Gardner, J. O. Hagen, R. Hock, G. Kaser, C. Kienholz, E. S. Miles, G. Moholdt, N. Mölg, F. Paul, V. Radić, P. Rastner, B. H. Raup, J. Rich, M. J. Sharp, L. M. Andreassen, S. Bajracharya, N. E. Barrand, M. J. Beedle, E. Berthier, R. Bhambri, I. Brown, D. O. Burgess, E. W. Burgess, F. Cawkwell, T. Chinn, L. Copland, N. J. Cullen, B. Davies, H. De Angelis, A. G. Fountain, H. Frey, B. A. Giffen, N. F. Glasser, S. D. Gurney, W. Hagg, D. K. Hall, U. K. Haritashya, G. Hartmann, S. Herreid, I. Howat, H. Jiskoot, T. E.

- Khromova, A. Klein, J. Kohler, M. König, D. Kriegel, S. Kutuzov, I. Lavrentiev, R. Le Bris, X. Li, W. F. Manley, C. Mayer, B. Menounos, A. Mercer, P. Mool, A. Negrete, G. Nosenko, C. Nuth, A. Osmonov, R. Pettersson, A. Racoviteanu, R. Ranzi, M. A. Sarikaya, C. Schneider, O. Sigurdsson, P. Sirguey, C. R. Stokes, R. Wheate, G. J. Wolken, L. Z. Wu, F. R. Wyatt, The randolph glacier inventory: A globally complete inventory of glaciers. *J. Glaciol.* **60**, 537–552 (2014).  
[doi:10.3189/2014JoG13J176](https://doi.org/10.3189/2014JoG13J176)
62. C. E. Telteu, H. Müller Schmied, W. Thiery, G. Leng, P. Burek, X. Liu, J. E. S. Boulange, L. S. Andersen, M. Grillakis, S. N. Gosling, Y. Satoh, O. Rakovec, T. Stacke, J. Chang, N. Wanders, H. L. Shah, T. Trautmann, G. Mao, N. Hanasaki, A. Koutroulis, Y. Pokhrel, L. Samaniego, Y. Wada, V. Mishra, J. Liu, P. Döll, F. Zhao, A. Gädeke, S. S. Rabin, F. Herz, Understanding each other's models: An introduction and a standard representation of 16 global water models to support intercomparison, improvement, and communication. *Geosci. Model Dev.* **14**, 3843–3878 (2021).  
[doi:10.5194/gmd-14-3843-2021](https://doi.org/10.5194/gmd-14-3843-2021)
63. P. K. Sen, Estimates of the Regression Coefficient Based on Kendall's Tau. *J. Am. Stat. Assoc.* **63**, 1379–1389 (1968). [doi:10.1080/01621459.1968.10480934](https://doi.org/10.1080/01621459.1968.10480934)
64. K. Stahl, L. M. Tallaksen, J. Hannaford, H. A. J. Van Lanen, Filling the white space on maps of European runoff trends: Estimates from a multi-model ensemble. *Hydrol. Earth Syst. Sci.* **16**, 2035–2047 (2012). [doi:10.5194/hess-16-2035-2012](https://doi.org/10.5194/hess-16-2035-2012)
65. X. Zhou, X. Huang, H. Zhao, K. Ma, Development of a revised method for indicators of hydrologic alteration for analyzing the cumulative impacts of cascading reservoirs on flow regime. *Hydrol. Earth Syst. Sci.* **24**, 4091–4107 (2020). [doi:10.5194/hess-24-4091-2020](https://doi.org/10.5194/hess-24-4091-2020)
66. K. Timpe, D. Kaplan, The changing hydrology of a dammed Amazon. *Sci. Adv.* **3**, e1700611 (2017). [doi:10.1126/sciadv.1700611](https://doi.org/10.1126/sciadv.1700611) Medline
67. M. R. Allen, P. A. Stott, Estimating signal amplitudes in optimal fingerprinting, part I: Theory. *Clim. Dyn.* **21**, 477–491 (2003). [doi:10.1007/s00382-003-0313-9](https://doi.org/10.1007/s00382-003-0313-9)
68. Y. Tramblay, N. Rouché, J.-E. Paturel, G. Mahé, J.-F. Boyer, E. Amoussou, A. Bodian, H. Dacosta, H. Dakhlaoui, A. Dezetter, D. Hughes, L. Hanich, C. Peugeot, R. Tshimanga, P. Lachassagne, The African Database of Hydrometric Indices (ADHI). *Earth Syst. Sci. Data* **9**, 1–21 (2020). [doi:10.5194/essd-2020-281](https://doi.org/10.5194/essd-2020-281)